

1 **Properties of Inelastic Yielding Zones Generated by In-plane**
2 **Dynamic Ruptures: II. Detailed parameter-space study**

3

4 Shiqing Xu¹ , Yehuda Ben-Zion¹ , Jean-Paul Ampuero²

5

6 ¹Department of Earth Sciences, University of Southern California, Los Angeles, California, USA

7 ²Seismological Laboratory, California Institute of Technology, Pasadena, California, USA

8

9

10

11

12 *Geophysics Journal International*

13 In review, 2012

14

15

16

17

18

19 Short title: Dynamic rupture & Off-fault yielding II

20

21 Keywords: Dynamics and mechanics of faulting; Rheology and friction of fault zones;

22 Mechanics, theory, and modeling; Microstructures; Elasticity and anelasticity;

23 Fractures and faults

24 SUMMARY

25 We perform a detailed parameter-space study on properties of yielding zones
26 generated by 2D in-plane dynamic ruptures on a planar fault with different frictional
27 laws and parameters, different initial stress conditions, different rock cohesion, and
28 different contrasts of elasticity and mass density across the fault. The focus is on cases
29 corresponding to large strike-slip faults having high angle ($\Psi = 45^\circ$) to the maximum
30 compressive background stress. The simulations and analytical scaling results show
31 that for crack-like ruptures (1) the maximum yielding zone thickness T_{\max} linearly
32 increases with rupture distance L and the ratio T_{\max}/L is inversely proportional to
33 $(1+S)^2$ with S being the relative strength parameter; (2) the potency density ε_0^p
34 decays logarithmically with fault normal distance at a rate depending on the stress
35 state and S ; (3) increasing rock cohesion reduces T_{\max}/L , resulting in faster rupture
36 speed and higher inclination angle Φ of expected microfractures on the extensional
37 side of the fault. For slip pulses in quasi-steady state, T is approximately constant
38 along strike with local values correlating with the maximum slip velocity (or final slip)
39 at a location. For a bimaterial interface with $\Psi = 45^\circ$, the energy dissipation to
40 yielding contributes to developing macroscopically asymmetric rupture with the same
41 preferred propagation direction predicted for purely elastic cases with Coulomb
42 friction. When $\Psi = 10^\circ$, representative for thrust faulting, the energy dissipation to
43 yielding leads to opposite preferred rupture propagation. In all cases, Φ is higher on
44 average on the compliant side. For both crack and pulse ruptures with $\Psi = 45^\circ$, T
45 decreases and ε_0^p increases for conditions representing greater depth. Significant
46 damage asymmetry of the type observed across several large strike-slip faults likely
47 implies persistent macroscopic rupture asymmetry (unilateral cracks, unilateral pulses,
48 or asymmetric bilateral pulses). The results on various features of yielding zones
49 expected from this and other studies are summarized in a table along with
50 observations from the field and laboratory experiments.

51

52 **1. INTRODUCTION**

53 The internal structure of fault zones reflects processes and conditions that have
54 operated during the fault history, and can affect various aspects of earthquakes and
55 seismic radiation in the future. It is therefore important to understand the relations
56 between properties of yielding zones around faults and different types of fault motion
57 (e.g. crack/pulse ruptures and aseismic failure on planar and rough surfaces). The goal
58 of this work is to contribute toward such understanding with a systematic
59 investigation of characteristics of yielding zones generated by dynamic ruptures on a
60 planar frictional interface. Xu *et al.* (2012), referred to hereafter as paper I, described
61 the computational method and defined several measures that can be used to quantify
62 properties of yielding zones using example results. In this companion paper we
63 perform a detailed parameter-space study on various features of off-fault yielding
64 generated by different types of dynamic ruptures associated with different frictional
65 laws and parameters, different initial conditions, and different elastic and cohesion
66 parameters of the surrounding media.

67 The example results in paper 1 and previous studies (e.g. Ben-Zion & Shi, 2005;
68 Templeton & Rice, 2008) demonstrated that the rupture style (crack vs. pulse) and
69 angle Ψ of the background maximum compressive stress relative to the fault
70 influence strongly the distribution of off-fault yielding zones. In section 2 of this
71 paper we investigate the roles of other parameters (relative strength parameter S , rock
72 cohesion, contrast of elasticity), and combinations of parameters corresponding to
73 certain physical situations, in controlling rupture dynamics and properties of yielding
74 zones including their location, extent, intensity, symmetry properties, microfracture
75 orientations and decay with fault-normal distance. The obtained results are used to
76 develop correlations and scaling relations among different manifestations of yielding
77 zones. In section 3 the findings are discussed in relation to other models (e.g., fault
78 motion on a rough surface) and observations from the field and the laboratory. The
79 results provide improved criteria for interpreting various features of yielding zones
80 around large strike-slip faults in terms of properties and conditions of earthquake
81 ruptures on the faults.

82

83 **2. DETAILED PARAMETER-SPACE STUDY**

84 Fig. 1a presents the geometry and several basic ingredients of the employed model.
85 Fig. 1b illustrates aspects of a model with fault roughness that will be discussed in
86 comparison with the obtained results. Since pulse-like ruptures are more sensitive
87 than crack-like ruptures to small changes of nucleation procedure, initial stress state,
88 fault frictional properties and other ingredients (e.g. Zheng & Rice, 1998; Ampuero &
89 Ben-Zion, 2008; Shi *et al.*, 2008; Dunham *et al.*, 2011a), we mainly use crack ruptures
90 to clarify the basic effects of various parameters. Results from both rupture styles will
91 be presented only when additional distinct features are seen for rupture pulses. We are
92 primarily interested in yielding zones associated with large strike-slip faults, so the
93 angle Ψ will be generally fixed at 45° unless mentioned otherwise. For
94 convenience, Table 1 summarizes key equations from paper I that are used frequently
95 in this work. The parameters specifying material properties, friction laws, nucleation
96 procedure and viscoplasticity have same values as in paper I (Table 1), except in cases
97 of bimaterial ruptures where the elastic moduli and mass density of medium 2 are
98 reduced. As in paper I, we provide normalized values of physical quantities.

99

100 **2.1 Influence of the S parameter**

101 The relative strength parameter S , defined as the ratio between strength excess
102 and dynamic stress drop (Eq. T1), is a key quantity connecting the background initial
103 stress with fault frictional properties (Andrews, 1976; Das & Aki, 1977). In natural
104 fault settings the S parameter may vary with the ratio of differential stress to the
105 confining pressure, the values of the static and dynamic friction coefficients, and
106 changing strike of fault segments in an approximately uniform regional stress field
107 (e.g. Lockner & Beeler, 2002; Shi *et al.*, 2008; Oglesby *et al.*, 2008). As in paper I, we
108 consider the range of values $S > 1.77$ to generate ruptures with subshear speed,
109 which is typical for most earthquakes. For the following investigation, the rock
110 cohesion is set at $c = 0$.

111 To carefully investigate how the S parameter can influence the yielding zone

112 properties, we choose the size of the applied nucleation zone L_{nucl} somewhat larger
 113 than the critical value L_c leading to dynamic instability (Palmer & Rice, 1973):

$$114 \quad L_c = \frac{16}{3\pi} \frac{\mu G_c}{(\tau_0 - \tau_d)^2}, \quad (1a)$$

115 where μ is the shear modulus, G_c is the fracture energy, and Poisson's ratio is
 116 assumed to be 0.25. We then fix the ratio of the applied nucleation size L_{nucl} to the
 117 critical size L_c , so that comparable amount of energy is released in rupture nucleation
 118 for cases with different S values. The fracture energy evaluated from the evolution of
 119 stress as a function of slip during the breakdown process for slip-weakening friction
 120 (SWF) is $G_c = (1/2) |\sigma_n| (f_s - f_d) D_c$, where D_c is the slip-weakening distance.

121 The critical size can be rewritten as

$$122 \quad L_c = \frac{8}{3\pi} \frac{\mu D_c}{|\sigma_n| (f_s - f_d)} (1 + S)^2. \quad (1b)$$

123 As the S value increases, the magnitude of the background normal stress has to
 124 increase to retain a comparable amount of released energy over the same nucleation
 125 length.

126

127 **2.1.1 Yielding zone extent and decay form**

128 Figure 2 shows the distribution of plastic strain for crack-like rupture cases
 129 associated with different S values. As seen, the extent of the plastic yielding zone is
 130 relatively wide when the S value is relatively low but can be highly suppressed when
 131 S becomes high. This is consistent with results of Templeton & Rice (2008) for cases
 132 where off-fault plastic yielding primarily occurs on the same side (i.e. the extensional)
 133 of the fault. Templeton & Rice (2008) attributed this extent dependence on S partly to
 134 the closeness of initial stress state to yielding level ($CF = \tau_{\text{max}}^0 / \sigma_Y^0$) as a function of S .
 135 We provide a quantitative explanation of the effect of S on the extent of the off-fault
 136 yielding zone in the Section 2.1.2.

137 Next we use the procedure described in paper I to investigate the off-fault decay
138 of the potency density ε_0^p . We examine the variation of ε_0^p in the fault normal
139 direction and define the thickness T of the yielding zone as the distance from the
140 fault where ε_0^p decreases to zero. In Figure 3 the sampling locations along the fault
141 strike are mapped into different colors (see inset in Figure 3a): each color represents a
142 trace normal to the fault strike, in the extensional side, starting from $X = 100L_0$
143 (blue) and ending at $X = 220L_0$ (red). The choice of the starting and ending points
144 ensures that the selected range is neither within the nucleation zone nor too close to
145 the rupture tip.

146 As shown in Figures 3b-3d, there are three distance ranges where the off-fault
147 variation of ε_0^p follows distinct patterns. In region (1) the yielding zone is affected
148 strongly by the artificial nucleation procedure (see inset in Fig. 3b) and is therefore
149 excluded from detailed analysis. Once the rupture propagates away from that region
150 ε_0^p may occur on both sides of the fault, but the summed value from both sides
151 asymptotically approaches at zero distance a constant related to the breakdown
152 process (inset in Fig. 3b). This feature is observed in all examined cases (a)-(d).

153 In the region labeled (2) in Fig. 3c, representing most of the off-fault distance
154 range where ε_0^p remains non-zero, there is a linear relation between ε_0^p and
155 $\log(d_\perp)$ over the examined (one order of magnitude) range of d_\perp . This logarithmic
156 decay is observed in all presented cases (Figs. 3a-3d), consistent with the results of
157 paper I and Yamashita (2000). The slope of the logarithmic decay for each case does
158 not depend on the sampling location (reflected by the sub-parallel color stripes), but it
159 clearly varies for different rupture cases. The latter variation can be explained by the
160 variable stress state which mainly determines the maximum value of ε_0^p close to the
161 fault (the intercept with the vertical axis), and by the S parameter which controls the
162 thickness of the yielding zone (the intercept with the horizontal axis).

163 As d_{\perp} continues to increase beyond some point, ε_0^p rapidly tapers to zero in a
 164 final third regime. We find a linear relation between the thickness of the yielding zone
 165 and the along-strike distance from the hypocenter (inset in Fig. 3d). This feature is
 166 consistent with the large scale view in Figure 2 (which is usually difficult to obtain in
 167 the field) that the off-fault yielding zones for the simulated crack cases have a
 168 triangular shape.

169

170 **2.1.2 Theoretical scaling relation**

171 How far the activated off-fault yielding zone can extend depends on the
 172 interaction between the background stress field σ_{ij}^0 and the slip-induced incremental
 173 stress field $\Delta\sigma_{ij}$ at some transitional distance range from the rupture tip where the
 174 two stress fields have comparable magnitude. Following Ben-Zion & Ampuero (2009),
 175 we develop a scaling relation between yielding zone thickness and the S parameter
 176 with order of magnitude quantities. Based on the singular crack model (e.g. Freund,
 177 1990), the incremental stress field $\Delta\sigma_{ij}$ in the vicinity of the crack tip can be
 178 described as:

$$179 \quad \Delta\sigma_{ij} = \frac{K_{II}^d}{\sqrt{2\pi r}} \Sigma_{ij}(\theta, v_r) + \begin{bmatrix} 0 & -\Delta\tau \\ -\Delta\tau & 0 \end{bmatrix} + O(\sqrt{r}), \quad (2)$$

180 where r and θ are polar coordinates with the origin at the crack tip (Fig. 2d),
 181 $\Delta\tau = \tau_0 - \tau_d$ is the stress drop, $K_{II}^d = k_{II}(v_r)\Delta\tau\sqrt{L}$ is the dynamic stress intensity
 182 factor with $k_{II}(v_r)$ being a universal function of rupture speed v_r , L denoting the
 183 half length of the crack (e.g. Broberg, 1999).

184 At the farthest distance r_{\max} from the rupture tip where off-fault yielding can be
 185 activated, the total stress field $\sigma_{ij} = \sigma_{ij}^0 + \Delta\sigma_{ij}$ is expected to just satisfy the yielding
 186 criterion for cohesionless rocks (Xu *et al.*, 2012):

$$187 \quad \sqrt{\sigma_{xy}^2 + (\sigma_{xx} - \sigma_{yy})^2 / 4} = -0.5(\sigma_{xx} + \sigma_{yy})\sin(\phi), \quad (3)$$

188 where ϕ is the internal friction angle. Writing σ_{ij}^0 and $\Delta\tau$ (normalized by σ_0) as
 189 functions of S and fault friction coefficients for $\Psi = 45^\circ$, using Eq. (2) to express
 190 $\Delta\sigma_{ij}$ as functions of $k_{II}(v_r)$, $\Delta\tau$, $\sqrt{L/r_{\max}}$ and $\Sigma_{ij}(\theta, v_r)$, and using the obtained
 191 expression for σ_{ij} in Eq. (3), we have

$$192 \quad \frac{r_{\max}}{L} = \eta \frac{k_{II}^2(v_r) \cdot A^2}{(1+S)^2}, \quad (4)$$

193 where η is a factor of order 1 (to be determined numerically) and A is a
 194 dimensionless quantity depending on $\Sigma_{ij}(\theta, v_r)$, friction coefficients and ϕ .

195 Projecting r_{\max} on the fault normal direction to estimate the maximum yielding zone
 196 thickness, T_{\max} , we get

$$197 \quad \frac{T_{\max}}{L} = \eta \frac{k_{II}^2(v_r) \cdot A^2 \cdot |\sin(\theta)|}{(1+S)^2}. \quad (5)$$

198 For any v_r , we can search for a value of θ that maximizes T_{\max}/L in Eq. (5).

199 Assuming $v_r = 0.827c_s$ typical for our cases, we get $\theta \approx -130^\circ$. This is consistent
 200 with the simulation results (see the yielding pattern near the rupture tips in Fig. 2,
 201 noting the vertical exaggeration of factor 3.75). Figure 4 shows a comparison between
 202 the numerical simulation results and Eq. (5) with $v_r = 0.827c_s$ and $\theta \approx -130^\circ$. For
 203 simplicity, we also adopt $k_{II}(v_r = 0.827c_s) \approx 0.375$ (Broberg, 1999, Fig. 6.9.8). The
 204 prediction with $\eta = 1$ (corresponding exactly to the theoretical solution)
 205 underestimates the ratio T_{\max}/L (dashed line in Fig. 4). Using a correction factor
 206 $\eta = 1.72$ provides a good agreement between the singular crack model with
 207 prescribed rupture process and the non-singular numerical results associated with
 208 spontaneous rupture and SWF.

209 A more detailed analysis may employ simulations with additional low values of S
 210 (before leading to supershear ruptures) or very high S values. At the former limit,

211 additional terms of Eq. (2) (i.e. those included in $O(\sqrt{r})$) may have to be considered,
 212 because when T_{\max}/L is expected to be fairly high (relatively) the above analyzed
 213 terms may not be sufficient to dominate the contribution to $\Delta\sigma_{ij}$. At the latter limit
 214 when T_{\max}/L is expected to be very low, Eq. (5) will reduce to

215
$$\frac{T_{\max}}{L} \propto \frac{1}{S^2}. \quad (6)$$

216 In this limit the finite size of the rupture tip cohesive zone, which is ignored in Eq. (2),
 217 should become important. In addition, this limit may approximate the case examined
 218 by Poliakov *et al.* (2002) for semi-infinite cracks ($L \rightarrow \infty$) with almost zero stress
 219 drop ($S \rightarrow \infty$).

220 We note that the scaling relations given by Eqs. (5) and (6) do not apparently
 221 depend on the absolute value of the stress field or any length scale, but rather imply a
 222 dependence of one non-dimensional quantity on another. These scaling implications,
 223 along with the previously reported self-similar slip profiles in paper I, can help
 224 identify crack-like earthquake ruptures based on field data, and may be useful for
 225 jointly constraining (or inferring) the remote stress field and/or fault frictional
 226 properties. As noted by Ben-Zion & Ampuero (2009), theoretical estimates of
 227 T_{\max}/W for pulses of width W can be derived in analogous fashion, with an
 228 appropriate function $f_{II}(v_r, v_h)$ dependent also on the speed of the healing front v_h .

229

230 **2.2 Influence of rock cohesion**

231 Several studies showed that the assumed value of rock cohesion can influence
 232 rupture dynamics and off-fault yielding (e.g. Ben-Zion & Shi 2005; Duan 2008; Ma &
 233 Andrews 2010). The effective value of this quantity usually varies with rock type and
 234 confining pressure, and depends strongly on the initial rock damage (e.g. Scholz, 2002;
 235 Jaeger *et al.*, 2007). Rock cohesion generally has two major effects that can influence
 236 the measurable properties associated with off-fault yielding. The first is directly

237 related to the extent of the yielding zone. As illustrated in Table 2, with the same
 238 initial stress state and nucleation procedure, increasing rock cohesion can reduce the
 239 size of the yielding zone and decrease, for crack ruptures, the ratio of yielding zone
 240 thickness to rupture distance. This direct effect is naturally expected from the adopted
 241 yielding criterion and is generally consistent with the appearance of c in the closeness
 242 to failure parameter of Templeton & Rice (2008):

$$243 \quad CF = \frac{\sqrt{(\sigma_{xx}^0 - \sigma_{yy}^0)^2 / 4 + (\sigma_{xy}^0)^2}}{-(1/2)(\sigma_{xx}^0 + \sigma_{yy}^0) \sin \phi + c \cos \phi}. \quad (7)$$

244 The second effect of rock cohesion is related to the microfracture orientation
 245 close to the fault. This effect operates through the evolving rupture speed that is
 246 correlated with the amount of off-fault yielding as a function of rock cohesion. To
 247 investigate the effect of rock cohesion on off-fault dynamic stresses, and hence
 248 yielding, we measure the expected microfracture orientation at a distance of $0.125L_0$
 249 (half spectral element) from the fault plane on the extensional side for $\Psi = 45^\circ$ and
 250 smooth the measurements over an along-strike length of $0.25L_0$ (one spectral
 251 element).

252 Figure 5a shows the predicted results for three friction coefficient ratios of SWF
 253 (with f_s fixed at 0.6), based on the non-singular crack model of Poliakov *et al.*
 254 (2002). For all three cases, the angle Φ of the expected microfractures relative to the
 255 fault (aligned to mode I type) monotonically increases with the normalized rupture
 256 speed v_r/c_s and asymptotically approaches 90° near the limit level c_R/c_s . Figure
 257 5b shows the variation of the normalized rupture speed v_r/c_s (solid curves with
 258 scale at the left vertical axis) and the inferred angle Φ (discrete markers with scale
 259 at the right vertical axis) obtained in the numerical simulations for three c values. For
 260 a given rock cohesion the variations of Φ are positively correlated with those of
 261 v_r/c_s . When comparing different cases with the same rupture propagation distance,
 262 the angle Φ increases with the rupture speed (associated with increasing rock
 263 cohesion).

264 The inset plot in Figure 5b explicitly illustrates the correlation of Φ with
265 v_r/c_s in the range indicated by the dashed box. The numerical results are generally
266 in good agreement with the analytic prediction for $f_d/f_s = 0.167$ (which
267 corresponds to $f_d = 0.1$ and $f_s = 0.6$). The systematic deviation of the numerically
268 inferred angle Φ from the analytic prediction may be explained by the essential
269 differences between the numerical and analytic models, e.g. with or without stress
270 relaxation once reaching the yielding criterion. We note that as c becomes higher,
271 reducing the influence of stress relaxation; the numerical results get closer to the
272 analytic prediction.

273

274 **2.3 Influence of material contrast across the fault**

275 So far the properties of dynamic ruptures and off-fault yielding zones have been
276 investigated in an isotropic homogeneous medium. However, large natural faults tend
277 to separate different rock bodies (e.g. McGuire & Ben-Zion 2005; Le Pichon *et al.*,
278 2005; Thurber *et al.*, 2006). In this section, we incorporate elasticity contrast across
279 the fault into our numerical procedure (Ampuero & Ben-Zion, 2008) and investigate
280 how the bimaterial effect can influence the generation and distribution of off-fault
281 yielding.

282 As in Ben-Zion & Shi (2005) and later studies, we find that the locations of the
283 off-fault yielding can be strongly affected by the existence of a bimaterial interface. In
284 an isotropic homogeneous medium, although the off-fault yielding zone is usually
285 asymmetrically distributed across the fault (for a single event), the partition pattern
286 with respect to the hypocenter is symmetric. However, this latter symmetry can be
287 broken by the presence of a material contrast across the fault. This and the different
288 stress concentrations between crack and pulse type ruptures lead to various changes in
289 yielding zones properties.

290 Figure 6 shows the distribution of plastic strain with 20% material contrast (see
291 paper I for definition) for crack-like ruptures generated using SWF. When $\Psi = 10^\circ$,
292 typical for thrust faults, plastic strain is dominantly distributed on the compliant side

293 in the positive direction, while it apparently extends to both sides of the fault in the
294 negative direction, showing an asymmetric pattern with respect to the hypocenter.
295 When $\Psi = 45^\circ$, typical for strike-slip faults, plastic strain is mainly distributed with
296 the employed parameters in the two extensional quadrants, generally following the
297 pattern in an isotropic homogeneous medium. However, the off-fault extent of the
298 yielding zone is wider on the stiff side (in the positive direction) than on the compliant
299 side (in the negative direction), consistent with the numerical results of Duan (2008).

300 Figure 7 shows the slip velocity profiles at different times and the estimated
301 rupture speed beyond the nucleation zone for the crack cases of Figure 6. The results
302 confirm that the rupture propagates as asymmetric bilateral crack for both cases,
303 consistent with the expectation that slip-weakening friction with relatively large
304 $f_s - f_d$ and smooth nucleation procedures lead to asymmetric bilateral cracks on a
305 bimaterial interface (e.g. Harris & Day, 1997; Shi & Ben-Zion, 2006; Rubin &
306 Ampuero 2007). In such cases, the direction with higher propagation speed and peak
307 slip velocity depends, along with the generation of off-fault yielding, strongly on Ψ .
308 When $\Psi = 10^\circ$, the left propagating tip has faster rupture speed and higher peak slip
309 velocity than the one propagating to the right (Figure 7a), in contrast to the prediction
310 for a purely elastic model in the subshear regime (e.g. DeDontney *et al.*, 2011). As
311 Ψ increases to 45° , the tip propagating to the right has (Figure 7b) faster speed and
312 higher peak slip velocity, consistent with the prediction for a purely elastic model (e.g.
313 Shi & Ben-Zion, 2006; Brietzke *et al.*, 2009).

314 The above differences in rupture and slip velocities may be explained by the
315 generation of off-fault yielding, whose distribution depends strongly on Ψ and on
316 the material contrast. When $\Psi = 10^\circ$, more plastic strain is distributed (Fig. 6a) on
317 the compliant side (in the positive direction) than on the stiff side (in the negative
318 direction). Therefore, although the right propagating rupture may be encouraged by
319 the tensile change of normal stress right behind the rupture front, the energy absorbed
320 by the larger off-fault yielding leads to lower rupture and peak slip velocities. When
321 $\Psi = 45^\circ$, the left propagating rupture generates larger plastic strain (Fig. 6b) and

322 compressive dynamic change of normal stress. Both effects lead to higher rupture and
323 slip velocities in the right (positive) direction. These features are generally consistent
324 with the numerical results of DeDontney *et al.* (2011) with off-fault elasto-plastic
325 response. We note that DeDontney *et al.* (2011) reported failed ruptures under
326 $\Psi = 45^\circ$ and unilateral ruptures in the positive direction under $\Psi = 35^\circ$, in contrast
327 to our asymmetric bilateral crack under $\Psi = 45^\circ$. These small differences may be
328 due to details associated with the employed material contrast, S parameter, and the
329 nucleation procedure. It should be mentioned that the bimaterial interface in our study
330 separates as in, e.g., Ben-Zion & Shi (2005) and DeDontney *et al.* (2011), materials of
331 different elastic moduli and mass density. The lower density on the compliant side
332 contributes to generation of higher plastic strain on that side compared to the stiff side.
333 This, in turn, leads to reversed preferred rupture direction under low Ψ values.
334 Duan (2008) used same mass density across the fault in his studies of bimaterial
335 ruptures and obtained higher magnitude of plastic strain on the stiff side in contrast to
336 our results and to those of DeDontney *et al.* (2011).

337 In addition to the asymmetry of off-fault yielding zones with respect to the
338 hypocenter, we wish to find more signatures that may help identify preferred rupture
339 direction or reflect the existence of a bimaterial fault. Among all the quantities that
340 have been investigated before, we find that off-fault microfracture orientation may be
341 a good indicator. Figure 8 shows the inferred results for the crack cases of Figure 6.
342 When $\Psi = 10^\circ$, the inferred angle Φ on the compliant side has a higher average
343 value than the one on the stiff side over the same off-fault distance range (see “C⁺” vs.
344 “C⁻” and “T⁻” vs. “T⁺” in Fig. 8a). Moreover, an interesting feature with a reversed
345 sign of Φ is observed in “C⁻”, probably reflecting the interaction between the
346 slip-induced stress change and the local dynamic change of normal stress. When
347 $\Psi = 45^\circ$, although the major plastic yielding switches to the extensional quadrants,
348 the inferred angle Φ still has a higher average value on the compliant side (“T⁻”)
349 than on the stiff side (“T⁺”). The results hold for off-fault yielding produced by single
350 asymmetric bilateral ruptures. The cumulative effect of multiple such ruptures with
351 different hypocenter locations is expected to produce off-fault yielding on both sides

352 of the fault, but still with a higher average angle of Φ on the compliant side than on
353 the stiff one.

354 Next we briefly discuss results for pulse-like bimaterial ruptures, whose dynamic
355 behavior is more sensitive to the generation of off-fault yielding. When $\Psi = 10^\circ$, the
356 rupture propagates as an asymmetric bilateral pulse with higher rupture and slip
357 velocities to the left (Figs. 9a and 10a). In contrast, as Ψ increases to 45° , the left
358 propagating pulse is arrested after some distance and the rupture eventually becomes a
359 unilateral pulse propagating to the right (Figs. 9b and 10b). For both $\Psi = 10^\circ$ and
360 $\Psi = 45^\circ$, the local T value correlates with the maximum slip velocity and final slip
361 (not shown here) at the same location (Figs. 9 and 10), consistent with the earlier
362 results of Ben-Zion & Shi (2005). The correlation with final slip can be related to the
363 analysis in section 2.1.2 and the previous work by Ben-Zion & Ampuero (2009) that
364 both the final slip and the yielding zone thickness are expected to scale with the pulse
365 width. The inferred angle Φ at a given propagation distance has higher average
366 value on the compliant side than on the stiff side for both cases (Fig. 11).

367 The above dynamic features can again be explained by the interaction between
368 the generation of off-fault yielding and the bimaterial effect through the angle Ψ .
369 However, we emphasize that the dynamic behavior of a propagating pulse is more
370 sensitive to off-fault yielding than that of a crack. With the same bimaterial fault
371 interface, the examined cracks continue to propagate bilaterally (asymmetrically) with
372 and without off-fault yielding, while the studied pulses can switch from being
373 asymmetrically bilateral to unilateral, depending on the amount of off-fault yielding.
374 The latter may be adjusted by changing the value of rock cohesion and/or S parameter.
375 This implies that, with a material contrast across the fault, the asymmetry of the
376 dynamic behavior and the associated off-fault yielding zones for pulse type ruptures
377 can be more prominent than that for cracks. In particular, the cumulative effect of the
378 case shown in Fig. 9b (with many hypocenter locations) is expected to produce much
379 more extensive off-fault yielding zones on the stiff side than on the compliant side, in
380 agreement with the numerical results of Ben-Zion & Shi (2005) based on Coulomb
381 type friction and various geological and seismological observations (e.g. Dor *et al.*,

382 2006, 2008; Lewis *et al.*, 2005, 2007; Mitchell *et al.*, 2011).

383

384 **2.4 Ruptures at different depth sections**

385 So far we investigated properties of rupture-induced inelastic yielding zones by
386 individually varying several controlling parameters including the background stress
387 state (in paper I), S parameter, rock cohesion and a possible contrast of rock elasticity
388 and density across the fault. Here we explore how combinations of these parameters
389 representing different depth sections can influence the generation and properties of the
390 inelastic yielding zones, with and without material contrast across the fault. In
391 particular, we define three typical depth sections, referred to as “shallow”,
392 “intermediate” and “deep”, considering that the on-fault initial shear and normal
393 stresses increase with depth. We also assume that the value of rock cohesion increases
394 with depth, in agreement with laboratory observations that damage healing and
395 cohesion increase with σ_n (e.g. Jaeger *et al.*, 2007; Johnson & Jia, 2005).

396

397 **2.4.1 Without material contrast across the fault**

398 We first quantify the effect of depth on crack-like ruptures (see caption of Figure
399 12). The angle Ψ is fixed at 45° , consistent with our focus on large strike-slip
400 faults, and the shear to normal stress ratio $\tau_0/(-\sigma_0)$ is fixed at 0.24, associated with
401 $S = 2.571$. To allow comparable amount of released energy to nucleate the rupture, we
402 also fix the ratio of the applied nucleation size L_{nucl} to the critical size L_c for
403 different cases, leading to smaller L_{nucl} with increasing depth (σ_0).

404 Figure 12 shows the plastic strain distribution for crack ruptures at the three
405 depth sections. As expected, the off-fault yielding zone for all three cases displays a
406 triangular shape that is mainly distributed in the extensional quadrant (only the right
407 half is shown due to the symmetry). However, the off-fault extent and magnitude of
408 the plastic strain vary with depth. The thickness of the yielding zone becomes
409 progressively narrower for conditions representing greater depth due to the increasing
410 rock cohesion. The magnitude of the plastic strain consistently increases with depth

411 due to the increasing background stress and dynamic stress drop. These features are
412 consistent overall with the early 2D results of Ben-Zion & Shi (2005) and Rice *et al.*
413 (2005), the more recent 3D simulation results of Ma (2008), Ma & Andrews (2010)
414 and Kaneko & Fialko (2011), and geological and seismological observations of
415 “flower-like” fault zone structure with depth (e.g. Rockwell & Ben-Zion, 2007, and
416 references therein). In particular, seismic trapped waves and related studies imply that
417 low velocity fault zone layers with considerable thickness are generally limited to the
418 top several kilometers of the crust (e.g., Ben-Zion *et al.* 2003; Lewis *et al.*, 2005;
419 Yang & Zhu 2010; Lewis & Ben-Zion, 2010; Yang *et al.* 2011).

420 We note that, as in Ben-Zion & Shi (2005) and later studies, we used a fairly low
421 cohesion value for shallow depth and relatively high c for deeper sections. It appears
422 that the assumed value of rock cohesion at different depth sections plays a more
423 important role in controlling the yielding zone extent than other depth-dependent
424 conditions such as the normal stress. This is anticipated by the scaling relation of Eq.
425 (5), indicating that when c is negligible, T is similar for depth ranges with similar S
426 parameter and rupture length, similar angle θ near the rupture tip (Fig. 2d), and
427 comparable rupture speeds. To verify this expectation we performed simulations with
428 same rock cohesion for different depth sections and found no prominent variation of
429 yielding zone thickness with depth, as long as the assumed c value remains a small
430 fraction (possibly zero) of σ_n at the shallowest examined depth. This is consistent with
431 the 3D numerical simulation by Ma & Andrews (2010) of crack-like rupture with
432 constant non-zero rock cohesion. As mentioned, laboratory data indicate that rock
433 cohesion should generally increase with depth (e.g. Jaeger *et al.*, 2007).

434 Figure 13 shows the expected microfracture orientation over certain off-fault
435 distance range for the crack cases of Fig. 12. The results generally display a similar
436 pattern for all three depth sections: Φ has a maximum value approaching 80° at a
437 fault normal distance $d_\perp \approx 0.4L_0$ and it gradually decreases to about 60° at
438 $d_\perp \approx 0.5L_0$ (Figs. 13a-13c). This similarity may be explained by the fact that the
439 dynamic stress drop is proportional to the background stress, and the total stress in Eq.

440 (T4) and plastic strain in Eq. (T5) increase linearly with depth. Despite the overall
441 similarity, the difference in the inclination angle Φ can still be observed by
442 investigating close-to-fault microfractures ($d_{\perp} = 0.125L_0$) due to rupture speed
443 variation with depth (Fig. 13d).

444 Figure 14 shows the plastic strain distribution for pulse type ruptures for
445 conditions representing two depth sections. Since the dynamic behavior of rupture
446 pulses is more sensitive to the generation of off-fault yielding (and many other
447 factors), only two depth sections, referred to as “shallow” and “intermediate”, are
448 used. The assumed values for S and c are slightly different from those used for the
449 crack ruptures but are self-consistent with variable depth conditions. In contrast to the
450 crack cases of Fig. 12, the yielding zone thickness for the pulse cases only slightly
451 decreases with depth and approaches a constant value along strike after its initial
452 growth. The mild depth variation might be explained by the tendency of the ruptures
453 generated with the employed rate-and-state friction law to evolve from steady-state to
454 self-similar pulse behavior with increasing dynamic stress drop while keeping all
455 other constitutive parameters unchanged (e.g. Zheng & Rice, 1998; Nielsen & Carlson,
456 2000; Ampuero & Ben-Zion, 2008). This is related to the fact that self-similar
457 (growing) ruptures usually produce broader yielding zones than pulse-like ruptures
458 that are approximately in steady-state (Ben-Zion & Shi, 2005; Xu *et al.*, 2012). The
459 case representing “intermediate” depth is associated with higher stress than the one
460 representing “shallow” section. As a result, the more energetic rupture pulse at greater
461 depth may partially counter or even overcome the effect of the increased c with depth.

462 Figure 15 shows the expected microfracture orientation for the pulse cases of Fig.
463 14. The inferred angle Φ has an average value around 70° at both depth sections,
464 and is slightly higher at the intermediate depth probably due to the faster rupture
465 speed at that depth (e.g. Rice *et al.*, 2005). Another interesting phenomenon is that the
466 angle Φ is approaching a constant as a function of fault normal distance
467 (characterized by the color) beyond $X = 200L_0$ at shallow depth (Fig. 15a). This and
468 the constant yielding zone thickness beyond $X = 200L_0$ in Fig. 14a imply that the

469 rupture pulse approaches quasi-steady propagation conditions around $X = 200L_0$.

470

471 **2.4.2 With material contrast**

472 Here various degrees of material contrast across the fault are added to represent
473 different depth ranges. Following Ben-Zion & Shi (2005), the degree of material
474 contrast γ decreases with depth: $\gamma = 20\%$ for “shallow”, $\gamma = 10\%$ for
475 “intermediate” and $\gamma = 5\%$ for “deep” sections (see paper I for definition). Except
476 for the variable value of γ , all other parameters are the same as in section 2.4.1.

477 Starting with crack type ruptures, we find that with variable γ the slip velocity
478 profiles still show some asymmetry with respect to the epicenter (similar to the results
479 in Fig. 7b), while the slip profiles and overall distribution of off-fault yielding zone
480 have a weak asymmetry with respect to the epicenter. The yielding zone thickness
481 linearly scales with the rupture distance at each depth, with a mildly higher growth
482 rate in the positive direction, and it systematically decreases with depth for each
483 propagation direction (Figure 16). The inferred angle Φ has a slightly higher
484 average value on the compliant side than on the stiff side over the same fault normal
485 distance range; this asymmetry becomes weaker with depth (Figure 17). Therefore,
486 such cases are not expected to produce clear asymmetric signals (co-seismic slip
487 profiles and generated yielding zones) that may be observed in geological studies.
488 One may expect that the cumulative effect of such cases with different hypocenter
489 locations will produce damage zones with a weak asymmetry across the fault at
490 shallow depth, and with almost symmetric distribution at deeper sections.

491 The corresponding results for pulse cases exhibit stronger differences for
492 conditions representing different depth sections of bimaterial faults. As shown in
493 Figure 18a, although the pulse rupture manages to propagate bilaterally for the
494 shallow depth case (compare with the reference case in Fig. 9b), the asymmetry of the
495 distributed yielding zone with respect to the hypocenter is still strong. In the positive
496 direction the pulse is associated with faster rupture speed and growing yielding zone

497 thickness, while in the negative direction it has slower rupture speed and more
498 localized off-fault yielding zone with an approximately constant thickness. The
499 difference in yielding zone thickness at $X = \pm 220L_0$ can be up to a factor two and
500 seems to continue to increase with propagation distance. Similarly, the asymmetry in
501 the local microfracture orientation with respect to the hypocenter is also prominent.
502 The inferred angle Φ has a higher average value and a smaller standard deviation on
503 the more compliant side than on the stiffer side (Figure 19a). For conditions
504 representing intermediate depth, the asymmetries of the yielding zone thickness and
505 local Φ are highly reduced (Figures 18b and 19b). The cumulative effect of multiple
506 pulse type ruptures on different depth sections of a bimaterial fault is expected to
507 produce a relatively wide-spread damage zone at shallow depth mainly on the stiff
508 side, and a highly localized relatively symmetric damage zone at greater depth. This is
509 generally consistent with the simulation results of Ben-Zion & Shi (2005).

510

511 **3. DISCUSSION**

512 As discussed and reviewed by various authors (e.g. Ben-Zion & Sammis, 2003;
513 Wilson *et al.*, 2003; Mitchell & Faulkner, 2009; Yamashita, 2009), there are many
514 proposed fault models on the formation and development of fault zone structures.
515 Although these models generally agree on the overall structure and elements of active
516 fault zones (e.g. principal plane, fault core, damage zone), they may be distinguished
517 at different spatio-temporal scales and by some damage features that are specific to
518 certain mechanical processes. In the following subsections we attempt to synthesize
519 (Table 3) the findings from our parameter-space study on different characteristics of
520 yielding zones with theoretical and observational results of others.

521

522 **3.1 On faulting processes**

523 The mechanism of generating off-fault yielding zones in our study, by rapid
524 progression of an earthquake rupture tip along a pre-existing fault plane, is referred to
525 as the “fifth model” by Mitchell & Faulkner (2009). This is the dynamic counterpart

526 to their “third model” where off-fault damage is produced by the formation and
527 migration of a “process zone” around the tips of a quasi-statically growing fault. We
528 generally do not differentiate between these two models because they share many
529 predictions such as asymmetrically distorted stress field around the rupture or fault tip
530 (e.g. Vermilye & Scholz, 1998; Poliakov *et al.*, 2002). These models may be
531 distinguished based on features (not simulated here) likely to be specific to dynamic
532 ruptures such as pseudotachylytes (e.g. Wenk *et al.*, 2000, Di Toro *et al.*, 2005) or
533 pulverized rocks (e.g. Dor *et al.*, 2006; Mitchell *et al.*, 2011; Doan & Billi 2011).
534 More subtle features that depend on rupture speed, such as the degree of stress
535 distortion near rupture tip reflected by the microfracture orientation, and magnitude of
536 stress drop reflected by the off-fault extent of damage zone (e.g. Andrews, 1976; Rice,
537 1980; Sibson, 1989) are highly non-unique. For simplicity, we will call both models
538 of damage production around propagating rupture and/or fault tip the “process zone”
539 model (PZM) and assume that the fault plane generally remains planar.

540 Another fault model (referred to by Mitchell & Faulkner (2009) as the “fourth”
541 model) emphasizes the roughness of the fault surface and suggests that the off-fault
542 damage is due to the stress interaction and cycling over fault irregularities during
543 displacement (e.g. Scholz, 1987; Chester & Chester, 2000; Wilson *et al.*, 2003;
544 Dieterich & Smith, 2009). Depending on the fault surface model (e.g. roughness,
545 frictional properties), the resulting off-fault damage can have different attributes at
546 different scales. For convenience, we will call this model the rough fault model
547 (RFM). One outcome of this model is the prediction that the perturbed principal stress
548 σ'_{\max} can have higher magnitude and higher inclination angle relative to local fault
549 surface around a restraining bend than around a releasing bend (Fig. 1b), assuming the
550 two bends have comparable size (e.g. Chester & Fletcher, 1997; Griffith *et al.*, 2010).
551 Additional mechanisms for generation of fault zone damage, referred to by Mitchell &
552 Faulkner (2009) as the “first” and “second” models are, respectively, processes related
553 to fault initiation and interaction between different faults. These two processes are not
554 considered in our following discussion.

555 Table 3 summarizes results on signatures of fault damage from our
556 parameter-space study, along with expectations from other studies involving
557 quasi-static PZM and fault motion associated with the RFM. The items listed at the
558 top of Table 3 are various features that may be used to characterize different
559 controlling mechanisms and the associated damage zone structure. The items listed
560 vertically on the left give additional specifications for each fault model. The angle Ψ
561 is assumed to be moderate to high, consistent with our focus on large strike-slip faults.
562 A single dominant principal displacement surface in 2D approximation is typically
563 assumed. Damage structures involving multiple fault cores, intersection between
564 different faults, and various 3D effects would have features associated with
565 superposition of the discussed entries and additional interactions that are not
566 considered in this work. Various quantitative connections between faulting processes
567 and damage structure are discussed further below.

568

569 **3.2 Key signatures of PZM and RFM in yielding zones**

570 With our assumption on relatively high Ψ and failure criteria that depend on
571 normal stress, the PZM generally predicts for both quasi-static process and a single
572 dynamic rupture that the off-fault yielding zone is more prominent on the extensional
573 side of the fault (e.g. Yamashita, 2000; Poliakov *et al.*, 2002; Rice *et al.*, 2005;
574 Willson *et al.*, 2007). This prediction is consistent with observations of
575 asymmetrically distributed tensile cracks near the tips of shear fractures or
576 pre-existing cuts in analogue experiments (Misra *et al.*, 2009), tensile cracks along the
577 two extensional quadrants of a small fault (Lim, 1998), and tensile cracks along a
578 frictional interface sustaining dynamic rupture in laboratory experiments (Griffith *et al.*,
579 2009). Coupling this asymmetry with an assumed preferred propagation direction
580 of bimaterial ruptures was used to explain the prominent damage asymmetry observed
581 across several large strike-slip faults, with significantly more damage on the sides
582 with faster seismic velocity at depth (e.g. Dor *et al.*, 2006, 2008; Wechsler *et al.*, 2009;
583 Mitchell *et al.*, 2011).

584 There have been suggestions that damage asymmetry may be expected also for

585 macroscopically symmetric bilateral ruptures (Rubin and Ampuero, 2007; Duan,
586 2008). However, the results of DeDontney *et al.* (2011) and our study indicate that
587 significant damage asymmetry is unlikely to be generated by macroscopically
588 symmetric bilateral cracks for conditions representing shallow depth where the
589 damage asymmetry has been observed. As mentioned in the introduction of paper I,
590 this is consistent also with results of Duan (2008) with low cohesion. Considerable
591 damage asymmetry consistent with observations seems to require macroscopic rupture
592 asymmetry in the form of unilateral cracks (e.g. Fig. 5a of DeDontney *et al.*, 2011),
593 asymmetric bilateral pulses (e.g. this study, Fig. 19a), or unilateral pulses (e.g. Fig. 5a
594 of Ben-Zion & Shi, 2005; this study, Fig. 9b). This is discussed further in section 3.3.

595 The PZM also predicts that microfractures are asymmetrically oriented around
596 the rupture or fault tips, with lower and higher angles on the compressional and
597 extensional side, respectively. The predicted sets of microfractures for small and
598 immature faults (related to designation “A” in Table 3) have been observed in the field
599 (Vermilye & Scholz, 1998). For relatively large and mature faults that are seismically
600 active (related to designation “B” in Table 3), a mixture of predicted sets of
601 microfractures is likely to be observed due to overprinting involving multiple rupture
602 events nucleated at different locations. The dynamic effects of rapidly propagating
603 ruptures, for both crack and pulse types, may modify the microfracture orientation by
604 promoting higher inclination angle on the extensional side at higher rupture speed in
605 the subshear regime (e.g. Poliakov, *et al.*, 2002; Rice *et al.*, 2005). This has been
606 observed in laboratory experiments for the rupture speed range $0.7c_R < v_r < 0.85c_R$
607 (Ngo *et al.*, 2012), but the effect may be too subtle to observe in the field.

608 When considering different rupture types (crack vs. pulse) of PZM, specific
609 signatures are additionally predicted by the scaling relation between the macroscopic
610 properties of the yielding zone (e.g. shape, thickness) and kinematic properties of the
611 rupture (e.g. rupture length, slip and slip velocity). As mentioned, self-similar ruptures
612 (either cracks or pulses) are expected to produce for single events triangular-shape
613 damage zones (e.g. Andrews, 2005; Templeton & Rice, 2008), while nearly-steady

614 pulse-like ruptures produce more localized damage zones with approximately constant
615 or a slightly growing thickness (e.g. Ben-Zion & Shi, 2005; Dunham *et al.*, 2011a). A
616 triangular-shape damage zone may also be produced by quasi-statically expanding
617 cracks, and it has been observed at various positions along the trace of the Gozo fault
618 in Maltese islands (Kim *et al.*, 2004, Fig. 7a). The dynamic and quasi-static crack type
619 faulting processes may be distinguished by the ratio of maximum damage zone
620 thickness to crack length, if the stress drop during dynamic ruptures is usually less
621 than that during quasi-static processes involving fracturing intact rocks (Sibson, 1989).
622 Observations of more localized damage generated by nearly steady pulse ruptures
623 may provide information on rupture speed, stress drop and pulse width (Ben-Zion &
624 Ampuero, 2009), along with the maximum slip velocity at a position having a given
625 yielding thickness (Ben-Zion & Shi, 2005).

626 The general signatures of the RFM-promoted fault damage zones may be
627 characterized by “irregular” distribution of yielding zone properties along directions
628 parallel or normal to the general fault strike. Nevertheless, at certain sections of the
629 rough fault, some yielding zone properties may show correlations with the local
630 geometric or kinematic properties of the fault. Assuming small quasi-static
631 displacement and small amplitude-to-wavelength ratio, simple model calculations for
632 a wavy fault with a single spectral component predict off-fault yielding that is
633 symmetric with respect to the local fault plane and local damage extent that scales
634 with the wavelength of the fault surface (Chester & Chester, 2000). The local
635 microfracture orientation in potential yielding zones depends on the type of fault bend,
636 background stress state, and fault frictional properties.

637 For relatively weak faults with moderate to high Ψ , the perturbed stress field
638 induced by fault roughness may produce high-angle microfractures associated with
639 high-magnitude fault normal stress around restraining bends (designated by “C~” in
640 Figure 1b and Table 3), low-angle microfractures associated with possible fault
641 opening around releasing bends (designated by “T~” in Figure 1b and Table 3), and/or
642 strong rotation in principal stress axes (see Figure 1b for definition) near the convex
643 corners of the fault (Saucier *et al.*, 1992; Chester & Chester, 2000; Griffith *et al.*,

644 2010). More realistic quasi-static calculations incorporating fault roughness at many
645 scales is expected to produce complex distribution of yielding zones along the entire
646 fault, but not to change the basic features produced by recent failure events around
647 each spectral component at its characteristic scale. The forgoing predictions related to
648 fault roughness have been applied to explain the reversed sense of shear stress near
649 the SAF in the Cajon Pass area (Saucier *et al.*, 1992) and the observed fault-normal
650 and fault-parallel microfractures along the Punchbowl fault in southern California
651 (Wilson *et al.*, 2003).

652 With increasing fault displacement, large-scale geometrical asperities are
653 expected to become involved and rocks may undergo stress cycling by the
654 juxtaposition of different irregularities of various scales and types during the change
655 of fault configuration. This may lead to two long-term cumulative features. (1) The
656 average yielding zone thickness is expected to scale with the total displacement and
657 largest wavelength of fault roughness along the examined fault segment (Chester &
658 Chester, 2000; Savage & Brodsky, 2011). (2) An overprinting of microfractures is
659 expected to produce a mixture of low- and high-angle microfractures at an arbitrary
660 location inside the yielding zone, and the maximum microfracture density is expected
661 to correlate with the fault displacement (Wilson *et al.*, 2003; Mitchell & Faulkner,
662 2009).

663 All models predict a decay of microfracture density with distance from the
664 principal fault surface. The results of this study indicate that the functional form of the
665 decay is logarithmic over most of the yielding zone extent (e.g. Figure 3), consistent
666 with the numerical study of Yamashita (2000). In contrast, Dieterich & Smith (2009)
667 suggested based on quasi-static simulations of slip on a rough fault a power law decay
668 of damage with distance from the fault. Some studies on quasi-static deformation of a
669 wavy fault had an exponential component in the solution for the decay of the
670 perturbed stress field from the fault (Saucier *et al.*, 1992; Chester & Chester, 2000),
671 suggesting exponential damage decay in locations where this component dominates
672 the full solution. The functional forms used to fit field observations vary in different
673 studies. Vermilye & Scholz (1998) fitted microfracture density decay for several small

674 faults in New York State with a logarithmic form. Mitchell *et al.* (2011) used the
675 logarithmic form to fit the reduction of rock pulverization intensity with distance from
676 the main slip surface of the Arima-Takatsuki Tectonic line in Japan. Savage &
677 Brodsky (2011) used a power law to fit fracture density decay for small faults near
678 Santa Cruz, California. Mitchell & Faulkner (2009) used an exponential decay form
679 for the Atacama fault zone in northern Chile. The difference in fitting functions may
680 stem from a preference related to assumed models or intended use, or it may reflect
681 actual differences in the key operating processes associated with the different
682 examined locations.

683

684 **3.3 Mechanisms for damage generation off a bimaterial fault**

685 Several effects can contribute to asymmetric off fault damage distribution
686 produced by multiple earthquake ruptures on a planar bimaterial fault. The opposite
687 senses of normal stress changes near the rupture tips propagating in the opposite
688 directions can lead to the development unidirectional pulse or bilateral rupture with
689 asymmetric slip and rupture velocities (e.g. Shi & Ben-Zion, 2006; Ampuero &
690 Ben-Zion, 2008; Brietzke *et al.*, 2009). Since damage is promoted on the extensional
691 side for cases with high Ψ representing large strike slip faults, ruptures that are
692 unilateral or more pronounced in one direction, will produce asymmetric damage
693 across the fault.

694 As shown in Figures 6-7 and 9-10 and by DeDontney *et al.* (2011), in cases with
695 high Ψ the coupling of off-fault energy dissipation due to yielding contributes to the
696 asymmetry of bimaterial ruptures compared to purely elastic cases. (In cases with low
697 Ψ representing thrust faults, the off-fault energy dissipation can produce opposite
698 rupture asymmetry). The combined result is expected to produce for subshear ruptures
699 on large strike-slip faults a statistically preferred propagation in the positive direction
700 (Fig. 1a), associated with more prominent damage on the stiff side. The type of
701 damage generated may be shear, tensile, or a mixture of both, depending on the
702 adopted criteria and competition between different failure modes. We note that
703 although in some studies the elastically-predicted or modeled plastic strain is a shear

704 type failure, its generation in some regions may be associated with tensile stress or
705 normal stress close to tensile (e.g. Andrews & Ben-Zion, 1997; Ben-Zion & Huang
706 2002; Dalguer & Day 2009). Therefore this type of damage may be used as an
707 indicator for potential tensile stress, at least for some locations on the extensional side
708 and along the fault right behind the rupture tip in the positive direction (Duan, 2008).

709 Some damage asymmetry across a bimaterial interface can also be produced
710 under quasi-static loadings. This has been invoked to explain asymmetric tensile
711 micro-cracking near grain boundaries separating different minerals (e.g. Dey & Wang,
712 1981; Kranz, 1983). However, in such cases involving approximately planar
713 boundaries the damage is confined to the immediate vicinity of the interface. In cases
714 of large bimaterial faults with roughness, more extensive damage with potential
715 tensile cracking may occur quasi-statically during the interseismic period around
716 releasing bends (e.g. Chester & Chester 2000). However, this is expected to be
717 dominated by the roughness and hence produce approximately symmetric damage.

718 A related topic is the observation of pulverized rocks along several large
719 strike-slip faults (e.g. Dor *et al.*, 2006, 2008; Mitchell *et al.*, 2011). The pulverized
720 rocks were found to be strongly asymmetric with respect to the main slip zone, with
721 most pulverized rock bodies on the side with faster seismic velocity at depth. The
722 damage asymmetry documented in these studies extends over hundreds of meters, and
723 has been observed in places to be accompanied by across-fault asymmetry over scales
724 of km involving various geomorphic features (e.g. Dor *et al.*, 2008; Wechsler *et al.*,
725 2009). Several signatures of the observed pulverized rocks suggest that they are
726 produced under conditions associated with tensile stress (see Mitchell *et al.*, 2011, and
727 references therein). Experimental studies suggest that generation of pulverized rocks
728 require high dynamic strain rates (Doan & Gary, 2009; Doan & Billi, 2011).

729 The wide extent of the observed pulverized rocks, their observations in the
730 context of large bimaterial strike-slip faults, and their existence primarily on the side
731 with faster velocity at depth suggest that they are likely produced by repeated
732 predominantly unilateral or strongly asymmetric bilateral earthquake ruptures. Based
733 on the results of sections 2.3 & 2.4.2 that weakly asymmetric ruptures are not

734 expected to produce significant damage asymmetry and previous related studies, we
735 may conclude that strongly asymmetric fault zone damage that includes pulverized
736 rocks is likely generated by pulse-type ruptures with statistically-preferred
737 propagation direction, although we cannot exclude the unilateral or strongly
738 asymmetric crack-type ruptures (see discussion in section 3.2).

739

740 **3.4 Limitations of the presented results and potential future improvements**

741 We have used 2D simulations to explore changes of fault zone damage with
742 depth that is likely generated by dynamic ruptures. Our 2D simulations with the
743 adopted Mohr-Coulomb criterion do not account for the stress/strength gradient with
744 depth (Ma & Andrews, 2010), the effect of the intermediate principal stress in
745 influencing rock damage (Lockner & Beeler, 2002), the finite width of the
746 seismogenic zone and the free surface (Day, 1982; Ma & Andrews, 2010). In
747 particular, the finite seismogenic depth implies an upper limit on self-similar rupture
748 growth (Day, 1982). Concerning our results about the evolution of the plastic zone
749 thickness for self-similar and quasi-steady ruptures, this suggests that the extent of the
750 damage zone scales linearly with fault length up to a value proportional to the
751 seismogenic depth. More precisely, our results for $\Psi = 45^\circ$ (Fig. 4) imply that the
752 fault zone thickness saturates at a value of a few percent the seismogenic depth, which
753 is a few hundred meters. This provides a possible explanation for the observation that
754 fault zone thickness for faults with large cumulated slip is typically a few hundred
755 meters, independently of fault length (Mitchell & Faulkner, 2009; Savage & Brodsky,
756 2010).

757 In addition our 2D simulations do not properly reflect the sensitivity of the
758 Green's function to a local disturbance in 3D (Evans, 2000, chapter 2.4). Moreover,
759 we have adopted a simple setting of model parameters without introducing saturation
760 of the effective normal stress at some depth or implied scaling relation of the
761 slip-weakening distance with final slip (e.g. Rice, 1993; Abercrombie & Rice, 2005),
762 nor did we consider effects associated with pre-existing low velocity fault zone layer
763 (e.g. Harris & Day, 1997; Ben-Zion & Huang 2002; Huang & Ampuero 2011). These

764 limitations could accordingly affect our evaluation of the 3D structure of fault damage
765 zones. Given that many adopted yielding criteria in both 2D and 3D are
766 pressure-dependent (e.g. Templeton & Rice, 2008; Ma & Andrews, 2010) and the size
767 of potential off-fault failure zone may scale with the slip-weakening distance (Rice *et*
768 *al.*, 2005), our results should be augmented by a future related parameter-space study
769 using 3D simulations of crack- and pulse-like ruptures.

770 Only limited numerical simulations of dynamic ruptures along rough faults have
771 been performed so far, mainly with a focus on high-frequency radiation and basic
772 properties of off-fault yielding (e.g. Dunham *et al.*, 2011b; Shi & Day, 2011). As
773 indicated in Table 3 for this category, there are many yielding zone properties that are
774 not covered or explored by these studies, such as the competition between properties
775 of dynamic ruptures and generated yielding zones. Some results of dynamic rupture
776 models show no or little damage in the immediate vicinity of fault releasing bends
777 (Dunham *et al.*, 2011b, Fig. 3c) or fault kink that is oriented into the extensional
778 quadrant (Duan & Day, 2008, Fig. 13), in contrast to the quasi-static expectations for
779 a wavy fault (Chester & Chester, 2000). These and other issues should be clarified by
780 future simulations of ruptures on rough faults.

781 The simulations done in this study and related earlier works used off-fault
782 yielding in the form of plastic strain, rather than brittle damage as observed
783 geologically (e.g. Wilson *et al.*, 2003; Dor *et al.*, 2008; Mitchell & Faulkner 2009)
784 and seismologically (e.g. Lewis *et al.*, 2005; Allam & Ben-Zion, 2012) in the structure
785 of natural faults. Brittle damage is associated with permanent volumetric changes (e.g.
786 Jaeger *et al.*, 2007), and the reduction of elastic moduli in the damage zones can lead
787 to significant motion amplification (e.g. Spudich & Olsen, 2001; Peng & Ben-Zion,
788 2006) and additional dynamic feedback mechanisms not accounted for by plasticity.
789 Examining the effects of such mechanisms, and producing clearer predictions on
790 damage products that may be compared with in-situ observations, require simulations
791 that incorporate brittle damage. This will be done in a follow up work.

792

793 **Acknowledgements**

794 The study was supported by the National Science Foundation (grants EAR-0944066
795 and EAR-0908903) and the Southern California Earthquake Center (based on NSF
796 Cooperative Agreement EAR-0529922 and USGS Cooperative Agreement
797 07HQAC0026).

798

799 **References**

800 Abercrombie, R.E., & Rice, J.R., 2005. Can observations of earthquake scaling
801 constrain slip weakening?, *Geophys. J. Int.*, **162**, 406-424.

802 Allam, A.A. & Ben-Zion, Y., 2012. Seismic velocity structures in the Southern
803 California plate-boundary environment from double-difference tomography,
804 *Geophys. J. Int.*, in review.

805 Ampuero, J.-P. & Ben-Zion, Y., 2008. Cracks, pulses and macroscopic asymmetry of
806 dynamic rupture on a bimaterial interface with velocity-weakening friction,
807 *Geophys. J. Int.*, **173**, 674-692.

808 Andrews, D.J., 1976. Rupture velocity of plane strain shear cracks, *J. Geophys. Res.*,
809 **81**, 5679–5687.

810 Andrews, D.J., 2005. Rupture dynamics with energy loss outside the slip zone, *J.*
811 *Geophys. Res.*, **110**, B01307, doi:10.1029/2004JB003191.

812 Andrews, D.J. & Y. Ben-Zion, Y., 1997. Wrinkle-like slip pulse on a fault between
813 different materials, *J. Geophys. Res.*, **102**, 553–571.

814 Ben-Zion, Y., 2008. Collective behavior of earthquakes and faults:
815 Continuum-discrete transitions, progressive evolutionary changes, and different
816 dynamic regimes, *Rev. Geophys.*, **46**, RG4006, doi:10.1029/2008RG000260.

817 Ben-Zion, Y. & Ampuero, J.-P., 2009. Seismic radiation from regions sustaining
818 material damage, *Geophys. J. Int.*, **178**, 1351–1356,
819 doi:10.1111/j.1365-246X.2009.04285.x.

820 Ben-Zion, Y. & Huang, Y., 2002. Dynamic rupture on an interface between a
821 compliant fault zone layer and a stiffer surrounding solid, *J. Geophys. Res.*,
822 107(B2), 2042, doi:10.1029/2001JB000254.

823 Ben-Zion, Y., Peng, Z., Okaya, D., Seeber, L., Armbruster, J.G., Ozer, N., Michael, A.J.,
824 Baris, S. & Aktar, M., 2003. Shallow fault zone structure illuminated by trapped
825 waves in the Karadere-Duzce branch of the North Anatolian Fault, western Turkey,
826 *Geophys. J. Int.*, **152**, 699–717.

827 Ben-Zion, Y. & Sammis, C.G., 2003. Characterization of Fault Zones, *Pure Appl.*
828 *Geophys.*, **160**, 677–715.

829 Ben-Zion, Y. & Shi, Z., 2005. Dynamic rupture on a material interface with
830 spontaneous generation of plastic strain in the bulk, *Earth Planet. Sci. Lett.*, **236**,
831 486–496, doi:10.1016/j.epsl.2005.03.025.

832 Brietzke, G.B., Cochard, A. & Igel, H., 2009. Importance of biomaterial interfaces for
833 earthquake dynamics and strong ground motion, *Geophys. J. Int.*, **178**(2),
834 921–938.

835 Chester, F.M. & Chester, J.S., 2000. Stress and deformation along wavy frictional
836 faults, *J. Geophys. Res.*, **105**(B10), 23,421–23,430.

837 Chester, J.S. & Fletcher, R.C., 1997. Stress distribution and failure in anisotropic rock
838 near a bend on a weak fault, *J. Geophys. Res.*, **102**(B1), 693–708,
839 doi:10.1029/96JB02791.

840 Cowie, P.A. & Scholz, C.H., 1992a. Physical explanation for the displacement-length
841 relationship of faults using a post-yielding fracture mechanics model, *J. Struct.*
842 *Geol.*, **14**(10), 1133–1148.

843 Cowie, P.A., & Scholz, C.H., 1992b. Growth of Faults by Accumulation of Seismic
844 Slip, *J. Geophys. Res.*, **97**(B7), 11,085–11,095, doi:10.1029/92JB00586.

845 Dalguer, L.A. & Day, S.M., 2009. Asymmetric rupture of large aspect-ratio faults at
846 bimaterial interface in 3D, *Geophys. Res. Lett.*, **36**, L23307,
847 doi:10.1029/2009GL040303.

848 Das, S. & Aki, K., 1977. A numerical study of two-dimensional spontaneous rupture
849 propagation, *Geophys. J. Roy. Astr. S.*, **50**(3), 643–668,
850 doi:10.1111/j.1365-246X.1977.tb01339.x

851 Day, S.M., 1982. Three-dimensional finite difference simulation of fault dynamics:
852 Rectangular faults with fixed rupture velocity, *Bull. seism. Soc. Am.*, **72**: 705–727

853 DeDontney, N., Templeton-Barrett, E.L., Rice, J.R. & Dmowska, R., 2011. Influence
854 of plastic deformation on bimaterial fault rupture directivity, *J. Geophys. Res.*,
855 **116**, B10312, doi:10.1029/2011JB008417.

856 Dey, T.N. & Wang, C-Y., 1981. Some mechanisms of microcrack growth and
857 interaction in compressive rock failure, *Int. J. Rock Mech. Min. Sci.*, **18**:
858 199–209.

859 Dieterich, J.H. & Smith, D.E., 2009. Nonplanar faults: Mechanics of slip and off-fault
860 damage, *Pure Appl. Geophys.*, **166**(10), 1799–1815, doi:
861 10.1007/s00024-009-0517-y.

862 Di Toro, G., Nielsen, S. & Pennacchioni, G., 2005. Earthquake rupture dynamics
863 frozen in exhumed ancient faults, *Nature*, **436**, 1009–1012,
864 doi:10.1038/nature03910.

865 Doan, M.L. & Gary, G., 2009. Rock pulverization at high strain rate near the San
866 Andreas Fault, *Nat. Geosci.*, **2**, 709–712, doi:10.1038/ngeo640.

867 Doan, M.-L. & Billi, A., 2011. High strain rate damage of Carrara marble, *Geophys.*
868 *Res. Lett.*, **38**, L19302, doi:10.1029/2011GL049169

869 Dor, O., Ben-Zion, Y., Rockwell, T.K. & Brune, J.N., 2006. Pulverized Rocks in the
870 Mojave section of the San Andreas FZ, *Earth Planet. Sci. Lett.*, **245**, 642–654,
871 doi:10.1016/j.epsl.2006.03.034.

872 Dor, O., Yildirim, C., Rockwell, T.K., Ben-Zion, Y., Emre, O., Sisk, M. & Duman,
873 T.Y., 2008. Geologic and geomorphologic asymmetry across the rupture zones of
874 the 1943 and 1944 earthquakes on the North Anatolian Fault: possible signals for
875 preferred earthquake propagation direction, *Geophys. J. Int.*, **173**, 483–504, doi:
876 10.1111/j.1365-246X.2008.03709.x.

877 Duan, B. & Day, S.M., 2008. Inelastic strain distribution and seismic radiation from
878 rupture of a fault kink, *J. Geophys. Res.*, **113**, B12311,
879 doi:10.1029/2008JB005847.

880 Duan, B., 2008. Asymmetric off-fault damage generated by bilateral ruptures along a
881 bimaterial interface, *Geophys. Res. Lett.*, **35**, L14306,
882 doi:10.1029/2008GL034797.

- 883 Dunham, E.M., Belanger, D., Cong, L. & Kozdon, J.E., 2011a. Earthquake ruptures
884 with strongly rate-weakening friction and off-fault plasticity, 1: Planar faults,
885 *Bull. seism. Soc. Am.*, **101**(5), 2296–2307. doi:10.1785/0120100075.
- 886 Dunham, E.M., Belanger, D., Cong, L. & Kozdon, J.E., 2011b. Earthquake ruptures
887 with strongly rate-weakening friction and off-fault plasticity, 2: Nonplanar
888 faults, *Bull. seism. Soc. Am.*, **101**(5), 2308–2322, doi:10.1785/0120100076.
- 889 Evans, L.C., 1998. *Partial Differential Equations*, American Mathematical Society.
- 890 Freund, L.B., 1990. *Dynamic fracture mechanics*, Cambridge University Press.
- 891 Griffith, W.A., Rosakis, A.J., Pollard, D.D. & Ko, C.-W., 2009. Dynamic rupture
892 experiments elucidate tensile crack development during propagating earthquake
893 ruptures, *Geology*, **37**, 795–798, doi:10.1130/G30064A.
- 894 Griffith, W.A., Nielsen, S., Di Toro, G. & Smith, S.A.F., 2010. Rough faults,
895 distributed weakening, and off-fault deformation, *J. Geophys. Res.*, **115**, B08409,
896 doi:10.1029/2009JB006925.
- 897 Harris, R.A. & Day, S.M., 1997. Effects of a low-velocity zone on a dynamic rupture,
898 *Bull. seism. Soc. Am.*, **87**, 1267–1280.
- 899 Jaeger, J., Cook, N. & Zimmerman, R., 2007. *Fundamentals of Rock Mechanics*,
900 Fourth ed., Blackwell Publishing Ltd, Malden, Massachusetts.
- 901 Johnson, P.A. & Jia, X., 2005. Nonlinear dynamics, granular media and dynamic
902 earthquake triggering, *Nature*, **473**, 871–874.
- 903 Kaneko, Y. & Fialko, Y., 2011. Shallow slip deficit due to large strike-slip earthquakes
904 in dynamic rupture simulations with elasto-plastic off-fault response. *Geophys. J.*
905 *Int.*, **186**, 1389–1403, doi:10.1111/j.1365-246X.2011.05117.x
- 906 Kim, Y.-S., Peacock, D.C.P. & Sanderson, D.J., 2004. Fault damage zones. *J. Struct.*
907 *Geol.*, **26**, 503–517.
- 908 Kranz, R.L., 1983. Microcracks in rocks: a review, *Tectonophysics* **100**: 449–480.
- 909 Le Pichon, X., Kreemer, C. & Chamot-Rooke, N., 2005. Asymmetry in elastic
910 properties and the evolution of large continental strike-slip faults, *J. Geophys. Res.*,
911 **110**, Art. No.B03405.
- 912 Lewis, M. A. and Y. Ben-Zion, 2010. Diversity of fault zone damage and trapping

913 structures in the Parkfield section of the San Andreas Fault from comprehensive
914 analysis of near fault seismograms, *Geophys. J. Int.*, **183**, 1579-1595, doi:
915 10.1111/j.1365-246X.2010.04816.x.

916 Lewis, M.A, Ben-Zion, Y. & McGuire, J., 2007. Imaging the deep structure of the San
917 Andreas Fault south of Hollister with joint analysis of fault-zone head and direct
918 P arrivals, *Geophys. J. Int.*, **169**, 1028-1042, doi:
919 10.1111/j.1365-246X.2006.03319.x.

920 Lewis, M.A., Peng, Z., Ben-Zion, Y. & Vernon, F.L., 2005. Shallow seismic trapping
921 structure in the San Jacinto fault zone near Anza, California, *Geophys. J. Int.*,
922 **162**, 867–881.

923 Lim, S.J., 1998. Small strike slip faults in granitic rock: implications for three
924 dimensional models, *Masters Thesis*, Utah State University, Logan, Utah.

925 Lockner, D.A., & Beeler, N.M., 2002. Rock Failure and Earthquakes - Chapter 32,
926 *International Handbook of Earthquake and Engineering Seismology*, edited by
927 W.H.K. Lee, H. Kanamori, P.C. Jennings, and C. Kisslinger, pp. 505–537,
928 Academic Press, Amsterdam.

929 Ma, S., 2008. A physical model for widespread near-surface and fault zone damage
930 induced by earthquakes, *Geochem. Geophys. Geosyst.*, **9**, Q11009,
931 doi:10.1029/2008GC002231.

932 Ma, S. & Andrews, D.J., 2010. Inelastic off-fault response and three-dimensional
933 dynamics of earthquake rupture on a strike-slip fault, *J. Geophys. Res.*, **115**,
934 B04304, doi:10.1029/2009JB006382.

935 McGuire, J. & Ben-Zion, Y., 2005. High-resolution imaging of the Bear Valley section
936 of the San Andreas Fault at seismogenic depths with fault-zone head waves and
937 relocated seismicity, *Geophys. J. Int.*, **163**, 152–164, doi:
938 10.1111/j.1365-246X.2005.02703.x.

939 Misra, S., Mandal, N., Dhar, R. & Chakraborty, C., 2009. Mechanisms of deformation
940 localization at the tips of shear fractures: Findings from analogue experiments
941 and field evidence, *J. Geophys. Res.*, **114**, B04204, doi:10.1029/2008JB005737.

942 Mitchell, T.M., Ben-Zion, Y. & Shimamoto, T., 2011. Pulverized Fault Rocks and

943 Damage Asymmetry along the Arima-Takatsuki Tectonic Line, Japan, *Earth*
944 *Planet. Sci. Lett.*, **308**, 284–297, doi:10.1016/j.epsl.2011.04.023.

945 Mitchell, T.M. & Faulkner, D.R., 2009. The nature and origin of off-fault damage
946 surrounding strike-slip fault zones with a wide range of displacements: A field
947 study from the Atacama fault system, northern Chile. *J. Struct. Geol.*, **31**,
948 802–816.

949 Ngo, D., Huang, Y., Rosakis, A.J., Griffith, W.A. & Pollard, D.D., 2012. Off-fault
950 tensile cracks: A link between geological fault observations, lab experiments and
951 dynamic rupture models, *J. Geophys. Res.*, doi:10.1029/2011JB008577, in press.

952 Nielsen, S.B. & Carlson, J.M., 2000. Rupture pulse characterization: self-healing,
953 self-similar, expanding solutions in a continuum model of fault dynamics, *Bull.*
954 *seism. Soc. Am.*, **90**, 1480–1497.

955 Oglesby, D.D., Mai, P.M., Atakan, K. & Pucci, S., 2008. Dynamic models of
956 earthquakes on the North Anatolian fault zone under the Sea of Marmara: Effect
957 of hypocenter location, *Geophys. Res. Lett.*, **35**, L18302,
958 doi:10.1029/2008GL035037.

959 Palmer, A.C. & Rice, J.R., 1973. Growth of slip surfaces in progressive failure of
960 over-consolidated clay, *Proc. R. Soc. London, Ser. A.*, **332**, 527–548.

961 Peng, Z. & Ben-Zion, Y., 2006. Temporal changes of shallow seismic velocity around
962 the Karadere-Düzce branch of the North Anatolian Fault and strong ground
963 motion, *Pure. Appl. Geophys.*, **163**, 567–600, doi:10.1007/s00024-005-0034-6.

964 Poliakov, A.N.B., Dmowska, R. & Rice, J.R., 2002. Dynamic shear rupture
965 interactions with fault bends and off-axis secondary faulting, *J. Geophys. Res.*,
966 **107**, doi:10.1029/2001JB000572.

967 Rockwell, T. K. and Ben-Zion Y., 2007. High localization of primary slip zones in
968 large earthquakes from paleoseismic trenches: Observations and implications for
969 earthquake physics, *J. Geophys. Res.*, 112, B10304, doi:10.1029/2006JB004764.

970 Rice, J.R., 1980. The mechanics of earthquake rupture, in *Physics of Earth's Interior*,
971 edited by A. M. Dziewonski and E. Boschi, *Proc. Int. Sch. Phys. Enrico Fermi*,
972 **78**, 555–649.

973 Rice, J.R., 1993. Spatio-temporal Complexity of Slip on a Fault, *J. Geophys. Res.*,
974 **98**(B6), 9885–9907, doi:10.1029/93JB00191.

975 Rice, J.R., Sammis, C.G. & Parsons, R., 2005. Off-fault secondary failure induced by
976 a dynamic slip-pulse, *Bull. seism. Soc. Am.*, **95**(1), 109–134,
977 doi:10.1785/0120030166.

978 Rubin, A.M. & Ampuero, J.-P., 2007. Aftershock asymmetry on a bimaterial interface,
979 *J. Geophys. Res.*, **112**, B05307, doi:10.1029/2006JB004337.

980 Saucier, F., Humphreys, E. & Weldon II, R., 1992. Stress Near Geometrically
981 Complex Strike-Slip Faults: Application to the San Andreas Fault at Cajon Pass,
982 Southern California, *J. Geophys. Res.*, **97**(B4), 5081–5094,
983 doi:10.1029/91JB02644.

984 Savage, H.M. & Brodsky, E.E., 2011. Collateral damage: Evolution with displacement
985 of fracture distribution and secondary fault strands in fault damage zones, *J.*
986 *Geophys. Res.*, **116**, B03405, doi:10.1029/2010JB007665.

987 Scholz, C.H., 1987. Wear and gouge formation in brittle faulting, *Geology*, **15**,
988 493–495.

989 Scholz, C.H., 2002. *The Mechanics of Earthquakes and Faulting*, Cambridge Univ.
990 Press, New York.

991 Scholz, C.H., Dawers, N.H., Yu, J.-Z., Anders, M.H. & Cowie, P.A., 1993. Fault
992 Growth and Fault Scaling Laws: Preliminary Results, *J. Geophys. Res.*, **98**(B12),
993 21,951–21,961, doi:10.1029/93JB01008.

994 Shi, Z. & Ben-Zion, Y., 2006. Dynamic rupture on a bimaterial interface governed by
995 slip-weakening friction, *Geophys. J. Int.*, **165**, 469–484.

996 Shi, Z., Ben-Zion, Y. & Needleman, A., 2008. Properties of dynamic rupture and
997 energy partition in a solid with a frictional interface, *J. Mech. Phys. Solids*, **56**,
998 5–24.

999 Shi, Z. & Day, S.M., 2011. 3D simulations of dynamic rupture on rough faults, AGU
1000 Fall Meeting, Abstract **S54C-06**.

1001 Sibson, R.H., 1989. Earthquake faulting as a structural process, *J. Struct. Geol.*, **11**,
1002 1–14.

- 1003 Spudich, P. & Olsen, K.B., 2001. Fault zone amplified waves as a possible seismic
1004 hazard along the Calaveras Fault in central California, *Geophys. Res. Lett.*,
1005 **28**(13), 2533–2536, doi:10.1029/2000GL011902.
- 1006 Templeton, E.L. & Rice, J.R., 2008. Off-fault plasticity and earthquake rupture
1007 dynamics: 1. Dry materials or neglect of fluid pressure changes, *J. Geophys. Res.*,
1008 **113**, B09306, doi:10.1029/2007JB005529.
- 1009 Thurber, C., Zhang, H., Waldhauser, F., Hardebeck, J., Micheal, A. & Eberhart-Phillips,
1010 D., 2006. Three-Dimensional Compressional Wavespeed Model, Earthquake
1011 Relocations, and Focal Mechanisms for the Parkfield, California, Region *Bull.*
1012 *seism. Soc. Am.*, **96**(4B), S38–S49.
- 1013 Vermilye, J.M. & Scholz, C.H., 1998. The process zone: A microstructural view of
1014 fault growth, *J. Geophys. Res.*, **103**, 12,223–12,237, doi:10.1029/98JB00957.
- 1015 Wechsler, N., Rockwell, T.K. & Ben-Zion, Y., 2009. Analysis of rock damage
1016 asymmetry from geomorphic signals along the trifurcation area of the San-Jacinto
1017 Fault, *Geomorphology*, **113**, 82–96.
- 1018 Wenk, H.-R., Johnson, L.R. & Ratschbacher, L., 2000. Pseudotachylites in the eastern
1019 Peninsular ranges of California. *Tectonophysics*, **321**, 253–277.
- 1020 Willson, J.P., Lunn, R.J. & Shipton Z.K., 2007. Simulating spatial and temporal
1021 evolution of multiple wing cracks around faults in crystalline basement rocks, *J.*
1022 *Geophys. Res.*, **112**, B08408, doi:10.1029/2006JB004815.
- 1023 Wilson, J.E., Chester, J.S. & Chester, F.M., 2003. Microfracture analysis of fault
1024 growth and wear processes, Punchbowl Fault, San Andreas System, California, *J.*
1025 *Struct. Geol.*, **25**, 1855–1873.
- 1026 Xu, S., Ben-Zion, Y & Ampuero, J.-P., 2012. Properties of inelastic yielding zones
1027 generated by in-plane dynamic ruptures: 1. Model description and basic results,
1028 to be submitted to *Geophysical Journal International*.
- 1029 Yamashita, T., 2000. Generation of microcracks by dynamic shear rupture and its
1030 effects on rupture growth and elastic wave radiation, *Geophys. J. Int.*, **143**,
1031 395–406.
- 1032 Yamashita, T, 2009. Chapter 8 Rupture Dynamics on Bimaterial Faults and Nonlinear

1033 Off-Fault Damage, in Fault-Zone Properties and Earthquake Rupture Dynamics,
 1034 *Int. Geophys.*, vol. **94**, edited by E. Fukuyama., pp. 187–215, Academic Press
 1035 Yang, H. & Zhu, L., 2010. Shallow low-velocity zone of the San Jacinto fault from local
 1036 earthquake waveform modelling, *Geophys. J. Int.*, **183**, 421–432.
 1037 Yang, H., L. Zhu, and E. S. Cochran. 2011. Seismic structures of the Calico fault zone
 1038 inferred from local earthquake travel time modelling. *Geophys. J. Int.*, 186,
 1039 760-770.
 1040 Zheng, G. & Rice, J.R., 1998. Conditions under which velocity-weakening friction
 1041 allows a self-healing versus a crack-like mode of rupture, *Bull. seism. Soc. Am.*,
 1042 **88**, 1466–1483.

1043

1044 **Figure Captions**

1045 **Figure 1.** (a) Schematic diagram showing the migration of rupture tips along a planar
 1046 fault, modified from Scholz *et al.* (1993). “C” and “T” represent the
 1047 compressional and extensional quadrant(s), respectively. In the presence of a
 1048 material contrast across the fault, the slip direction on the compliant side will be
 1049 referred to as the positive direction, and the quadrants in the same or opposite
 1050 directions will be distinguished by “+/-” signs. (b) Schematic diagram of a rough
 1051 fault with geometric complexities, modified from Saucier *et al.* (1992) and
 1052 Chester & Fletcher (1997). For both (a) and (b), the big arrows indicate the
 1053 orientation of the far field background maximum compressive stress σ_{\max} while
 1054 the small thin arrows represent the orientation and relative magnitude (indicated
 1055 by the length) of the near-fault (dynamically or quasi-statically) perturbed
 1056 maximum compressive stress σ'_{\max} .

1057 **Figure 2.** Plastic strain distribution for crack-like ruptures with $\Psi = 45^\circ$ and
 1058 different values of S . The intensity of the plastic strain is quantified by the
 1059 seismic potency density $\varepsilon_0^p = \sqrt{2\varepsilon_{ij}^p \varepsilon_{ij}^p}$ (see Paper I). The background normal
 1060 stress σ_0 differs to preserve comparable energy release from the nucleation

1061 zone. In (d), r and θ are polar coordinates with origin at the moving rupture
 1062 tip, and ω is a conventional angle quantifying the incremental rate of yielding
 1063 zone thickness with the along-strike distance from the hypocenter (i.e.
 1064 $\tan(\omega) \approx \Delta T / \Delta X$).

1065 **Figure 3.** Off-fault decay of the seismic potency density ε_0^p vs. fault normal
 1066 distance d_{\perp} for crack-like ruptures associated with different S and σ_0 values.
 1067 The schematic diagram in (a) illustrates the employed mapping between sets of
 1068 colors and distance from hypocenter. The inset in (b) shows the variation of ε_0^p
 1069 from each side of the fault (or the summed value) along the strike. The inset plot
 1070 in (d) reproduces the result in a double-linear scale.

1071 **Figure 4.** Comparison of the numerical results and theoretical prediction of Eq. (5)
 1072 (with assumed $\theta = -130^\circ$ and $v_r = 0.827c_s$) on the scaling relation between
 1073 T_{\max} / L and S . Numerical results are obtained by first calculating $\Delta T / \Delta X$
 1074 based on the measurements in Fig. 3, and then converting it into angle ω to
 1075 calculate T_{\max} / L through the relation $T_{\max} / L = \sin(\omega) \sin(|\theta|) / \sin(|\theta| - \omega)$
 1076 (see angle definition in Fig. 2d).

1077 **Figure 5.** (a) Analytic prediction of close-to-fault microfracture orientation as a
 1078 function of rupture speed v_r with a fixed static friction coefficient $f_s = 0.6$,
 1079 based on the non-singular crack model of Poliakov *et al.*, (2002)
 1080 ($-R < x - v_r t < 0$, $y \approx 0^-$, with R being the size of process zone). (b) Variation
 1081 of numerically inferred close-to-fault microfracture orientation and rupture speed
 1082 along strike, for cases with different rock cohesion values. The inset shows the
 1083 comparison between the numerical results in the dashed box and the analytic
 1084 prediction in about the same selected range.

1085 **Figure 6.** Plastic strain distribution for crack-like ruptures on a bimaterial interface
 1086 with 20% contrast for (a) $\Psi = 10^\circ$ and (b) $\Psi = 45^\circ$. For both cases,

1087 $\sigma_{xy}^0 = 0.24\sigma_c$, $\sigma_{yy}^0 = -1.0\sigma_c$ and $c = 0.2\sigma_c$.

1088 **Figure 7.** Slip velocity profiles for the crack cases of Figure 6, with the generalized
1089 Rayleigh wave speed being $c_{GR} = 0.825c_s^{\text{fast}}$ for $\gamma = 20\%$.

1090 **Figure 8.** Inferred microfracture orientation for the crack cases of Figure 6 (see Fig.
1091 1a for quadrant notations).

1092 **Figure 9.** Plastic strain distribution for pulse-like ruptures on a bimaterial interface
1093 with 20% contrast for (a) $\Psi = 10^\circ$ and (b) $\Psi = 45^\circ$. For both cases,
1094 $\sigma_{xy}^0 = 1.04\sigma_c$, $\sigma_{yy}^0 = -4.0\sigma_c$ and $c = 0$.

1095 **Figure 10.** Slip velocity profiles for the pulse cases of Figure 9, with the generalized
1096 Rayleigh wave speed being $c_{GR} = 0.825c_s^{\text{fast}}$ for $\gamma = 20\%$.

1097 **Figure 11.** Inferred microfracture orientation for the pulse cases of Figure 9.

1098 **Figure 12.** Plastic strain distribution for crack-like ruptures at conditions representing
1099 different depth sections without material contrast across the fault. For all cases,
1100 $\tau_0 / (-\sigma_0) = 0.24$ or $S = 2.571$. Parameters for different depth sections are: (a)
1101 $\sigma_0 = -1.0\sigma_c$, $c = 0.2\sigma_c$; (b) $\sigma_0 = -1.62\sigma_c$, $c = 0.48\sigma_c$; (c) $\sigma_0 = -3.06\sigma_c$,
1102 $c = 1.2\sigma_c$.

1103 **Figure 13.** (a)-(c): Inferred microfracture orientation for the crack cases of Figure 12
1104 at different depth sections. (d) Correlation between the close-to-fault
1105 microfracture orientation and rupture speed at three typical depth sections.

1106 **Figure 14.** Plastic strain distribution for pulse-like ruptures at conditions representing
1107 different depth sections without material contrast across the fault. For both cases,
1108 $\tau_0 / (-\sigma_0) = 0.26$ or $S = 2.125$. Parameters for different depth sections are: (a)
1109 $\sigma_0 = -4.0\sigma_c$, $c = 0.8\sigma_c$; (b) $\sigma_0 = -6.0\sigma_c$, $c = 2.4\sigma_c$.

1110 **Figure 15.** Inferred microfracture orientation for the pulse cases of Figure 14 at
1111 different depth sections.

1112 **Figure 16.** Plastic strain distribution for crack-like ruptures at conditions representing
1113 different depth sections on a bimaterial interface. Except for the variable degree

1114 of material contrast, all the other parameters are as in Figure 12. Parameters for
 1115 material contrast at different depth sections are: (a) $\gamma = 20\%$, $c_{GR} = 0.825c_s^{\text{fast}}$;
 1116 (b) $\gamma = 10\%$, $c_{GR} = 0.873c_s^{\text{fast}}$; (c) $\gamma = 5\%$, $c_{GR} = 0.896c_s^{\text{fast}}$.

1117 **Figure 17.** Inferred microfracture orientation for the crack cases of Figure 16 at
 1118 different depth sections.

1119 **Figure 18.** Plastic strain distribution for pulse-like rupture at conditions representing
 1120 different depth sections on a bimaterial interface. Except for the variable degree
 1121 of material contrasts, all the other parameters are as in Figure 14. Parameters for
 1122 material contrast at different depth sections are: (a) $\gamma = 20\%$, $c_{GR} = 0.825c_s^{\text{fast}}$;
 1123 (b) $\gamma = 10\%$, $c_{GR} = 0.873c_s^{\text{fast}}$.

1124 **Figure 19.** Inferred microfracture orientation for the pulse cases of Figure 18.

1125

1126 Tables

1127 **Table 1. Key equations**

$S = \frac{\tau_s - \tau_0}{\tau_0 - \tau_d}$	(T1)
$\sigma_{xy}^0 = \frac{f_s + Sf_d}{1 + S} (-\sigma_{yy}^0)$	(T2)
$\sigma_{xx}^0 = \left[1 - \frac{2\sigma_{xy}^0}{\tan(2\Psi)\sigma_{yy}^0} \right] \sigma_{yy}^0$	(T3)
$\Psi = \frac{1}{2} \arccos \left[\frac{\sigma_{yy} - \sigma_{xx}}{\sqrt{(\sigma_{yy} - \sigma_{xx})^2 + 4\sigma_{xy}^2}} \right] \text{sgn}(\sigma_{xy})$	(T4)
$\Phi = \frac{1}{2} \arccos \left[\frac{-\varepsilon_{xx}^p}{\sqrt{(\varepsilon_{xx}^p)^2 + (\varepsilon_{xy}^p)^2}} \right] \text{sgn}(\varepsilon_{xy}^p)$	(T5)
τ_s & τ_d : static & dynamic shear strength of the fault; τ_0 : initial shear stress.	
f_s & f_d : static & dynamic friction coefficient ($f_s = 0.6$, $f_d = 0.1$).	

Ψ : angle of the maximum compressive stress relative to the fault (based on the stress tensor σ_{ij}), specified as the angle for the background stress if using σ_{ij}^0 .

Φ : angle of the expected microfracture (aligned to the mode-I type) relative to the fault (based on the plastic strain tensor ε_{ij}^p).

1128

1129

1130 **Table 2. Relation between the incremental rate of yielding zone thickness with**
1131 **along-strike distance from the hypocenter and rock cohesion c**

	$c = 0.0\sigma_c$	$c = 0.2\sigma_c$	$c = 0.4\sigma_c$	$c = 0.6\sigma_c$
$\Delta T / \Delta X$	0.0635	0.0364	0.0221	0.0139

1132

Table 3: Observable features of fault damage zones (in 2D approximation)

		Location	Spatial pattern and extent	Microfracture orientation [†]	Density decay	Scaling relation or correlation	Notes & References (this study = paper II)
PZM	Quasi-static (A&B)	in “C” (I ^d &II, minor) & “T” (I ^t &II, major)	T increases from the initiation point(s) towards fault growing direction (triangular shape)	$\Phi \approx 20^\circ$ in “C” and $\Phi \approx 70^\circ$ in “T”	logarithmic, exponential or power-law decay	$d_{\max} \propto L$; $d_0 \propto L$; $T_{\max} \propto L$; $\rho_{\max} \approx \text{const.}$, indep. of L	Crack Cowie & Scholz (1992a), Scholz <i>et al.</i> (1993), Vermilye & Scholz (1998), Mitchell & Faulkner (2009), Savage & Brodsky (2011)
	Dynamic	A: prominently in “T” (I ^t & II), might also in “C” (I ^d & II) B: on both sides	A: T increases from the hypocenter towards rupture propagation direction (triangular shape), usually narrower than that for a quasi-statically growing fault B: $T \approx \text{const.}$ (moderate to wide)	A: $\Phi < \Psi$ in “C”; $\Phi > \Psi$ in “T”, Φ (in “T”) increases with increasing v_r ($\sim 90^\circ$ when v_r approaches v_{lim}) or decreasing τ_d/τ_s ; sense of fault-parallel shear ahead of rupture tip can be reversed at high v_r . B: two clustered sets: $\Phi < \Psi$ (minor) and $\Phi > \Psi$ (major)	logarithmic decay (A&B)	A: $d_{\max} \propto L$; $T_{\max}/L \propto S^{-2}$ (S is relatively large); $\rho_{\max} \approx \text{const.}$, indep. of L ; B: ρ_{\max} grows with # of EQs (overprint ¹), might be upper bounded	Crack Cowie & Scholz (1992b), Scholz <i>et al.</i> (1993), Yamashita (2000), Poliakov <i>et al.</i> (2002), Andrews (2005), Templeton & Rice (2008), Ben-Zion & Ampuero (2009), Mitchell & Faulkner (2009), paper I (Figs. 7, 11, 13–15), this study (Figs. 2, 3–5, 12, 13)
			A: $T \approx \text{const.}$ (narrow), can increase towards rupture propagation direction B: $T \approx \text{const.}$ (narrow to moderate)			A: d & T correlates with v_{\max} and pulse width, usually approach const. but can grow with L B: overprint ¹ of ρ_{\max}	
	Dynamic + bimaterial	A: similar to the case w/o material contrast B: on both sides (“1”: stiff side, “2”: compliant side; “+/-” for particle motion direction on side 2/1)	similar to the case w/o material contrast (A&B), slightly-to-moderately more pronounced in “+” direction (A) or on the stiff side (B)	A: $\Phi_2^- > \Phi_1^+ > \Psi$ in “T”, $\Phi < \Psi$ in “C” B: similar to the case w/o material contrast; for the majority: $\Phi_2 > \Phi_1 > \Psi$	logarithmic decay with asymmetric slopes wrt. the hypocenter (A) or across the fault (B)	A: $d_{\max}^\pm \propto L^\pm$; $T_{\max}^\pm \propto L^\pm$; asymmetry of T & d wrt. the hypocenter correlates with γ ; B: T_1/T_2 correlates with γ	Crack Duan (2008), DeDontney <i>et al.</i> (2011), this study (Figs. 6–8, 16, 17)
A: $T^+ \approx \text{const.}$ (narrow to moderate), can grow with L^+ ; T^- depends, usually highly localized; B: T_1 (moderate) $\gg T_2$ (localized)			A: d^\pm & T^\pm correlate with v_{\max}^\pm ; $d^+ \approx \text{const.}$, might grow with L^+ ; d^- depends, usually rapidly tapers B: T_1/T_2 correlates with γ			Pulse Ben-Zion & Shi (2005), Ampuero & Ben-Zion (2008), this study (Figs. 9–11, 18, 19)	
RFM	Quasi-static	on both sides (A&B)	A: T fluctuates along strike, may be more extensive around “T~” than around “C~” B: $T \approx \text{const.}$	irregular: from fault parallel to fault normal when f is not very high; sense of fault-parallel shear near connex corner can be reversed with low f (A&B)	exponential or power-law decay (A&B)	A: $d_{\max} \propto \beta^{-2}$, indep. of L (L is large), $d_{\max} \propto L$ (L is small); $T \propto \lambda$, $\rho_{\max} \propto \lambda^{-\alpha}$ ($\alpha > 0$) B: $T \propto d$, also depends on λ_{\max} ; ρ_{\max} grows with d (overprint ²), might be upper bounded	Crack Saucier <i>et al.</i> (1992), Chester & Fletcher (1997), Chester & Chester (2000), Wilson <i>et al.</i> (2003), Dieterich & Smith (2009), Griffith <i>et al.</i> (2010)
	Dynamic	A: the overall location may agree well with that predicted by PZM B: on both sides	A: T fluctuates along strike, may show patterns of PZM along portions with low β ; damage may be absent in the immediate vicinity of “T~” B: $T \approx \text{const.}$ with fluctuation	several clustered sets, which are expected to reflect the competition between dynamic effect and local rough fault surface (A&B)	N.A. (A&B)	A: lack of macroscopic scaling relations at the present time; v_r anti-correlates with the slope of fault profile B: N.A.	Crack/Pulse Duan & Day (2008), Dumham <i>et al.</i> (2011b), Shi & Day (2011)

PZM = Process Zone Model (with approximately planar fault interface), RFM = Rough Fault Model. A single principal fault surface is assumed. The angle Ψ of the background maximum compressive stress relative to the fault is assumed to be moderate to high, representative for (but not limited to) large strike-slip faults.

[†] The orientation is described by the angle Φ of the measured (or inferred) microfractures (aligned to the mode-I type) relative to the fault.

A: in a short-term process (e.g. during a single seismic event or with small amount of displacement), B: in a long-term process (e.g. after multiple seismic cycles with variable hypocenter locations or with large cumulative displacement); “C”&“T”: compressional and extensional quadrants, respectively; “C~”&“T~”: restraining and releasing bends, respectively; I^d: dilatant microfractures (under compression), I^t: tensile microfractures (under transient tension); II: mode-II shear microfractures; T : damage zone thickness; d : displacement or seismic slip; d_0 : characteristic displacement on the trailing edge of process zone; L : fault half length or rupture distance; ρ : microfracture density or its equivalence (e.g. seismic potency density); v_r : rupture speed; τ_d : dynamic shear strength of the fault; τ_s : static shear strength of the fault; S : relative strength S parameter (see the text); v_{\max} : maximum slip velocity; γ : degree of material contrast; f : friction coefficient; β : roughness (e.g. rms slope) of fault profile; λ : wavelength of fault profile. Subscript “max” is used to specify the maximum value of a quantity (e.g. d_{\max} , T_{\max} , ρ_{\max}).

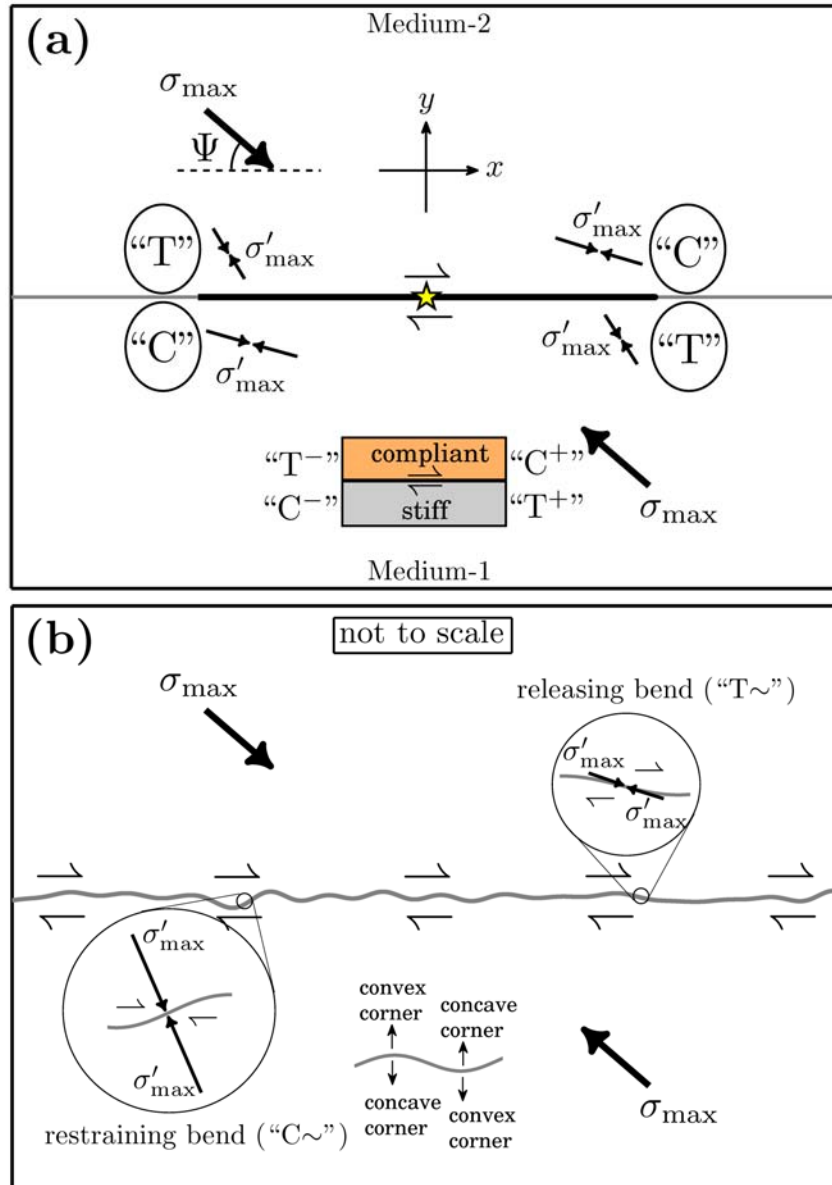


Figure 1

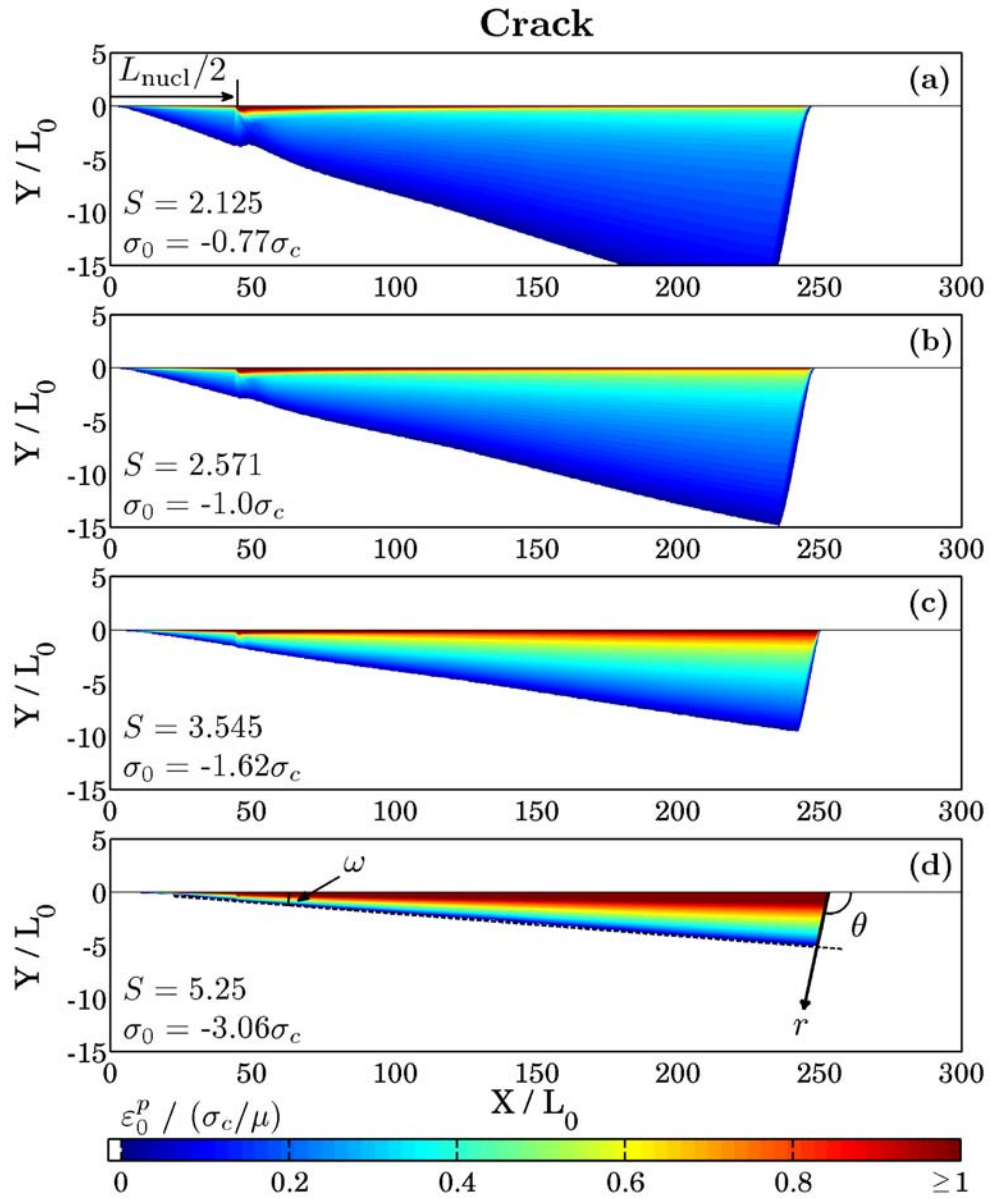


Figure 2

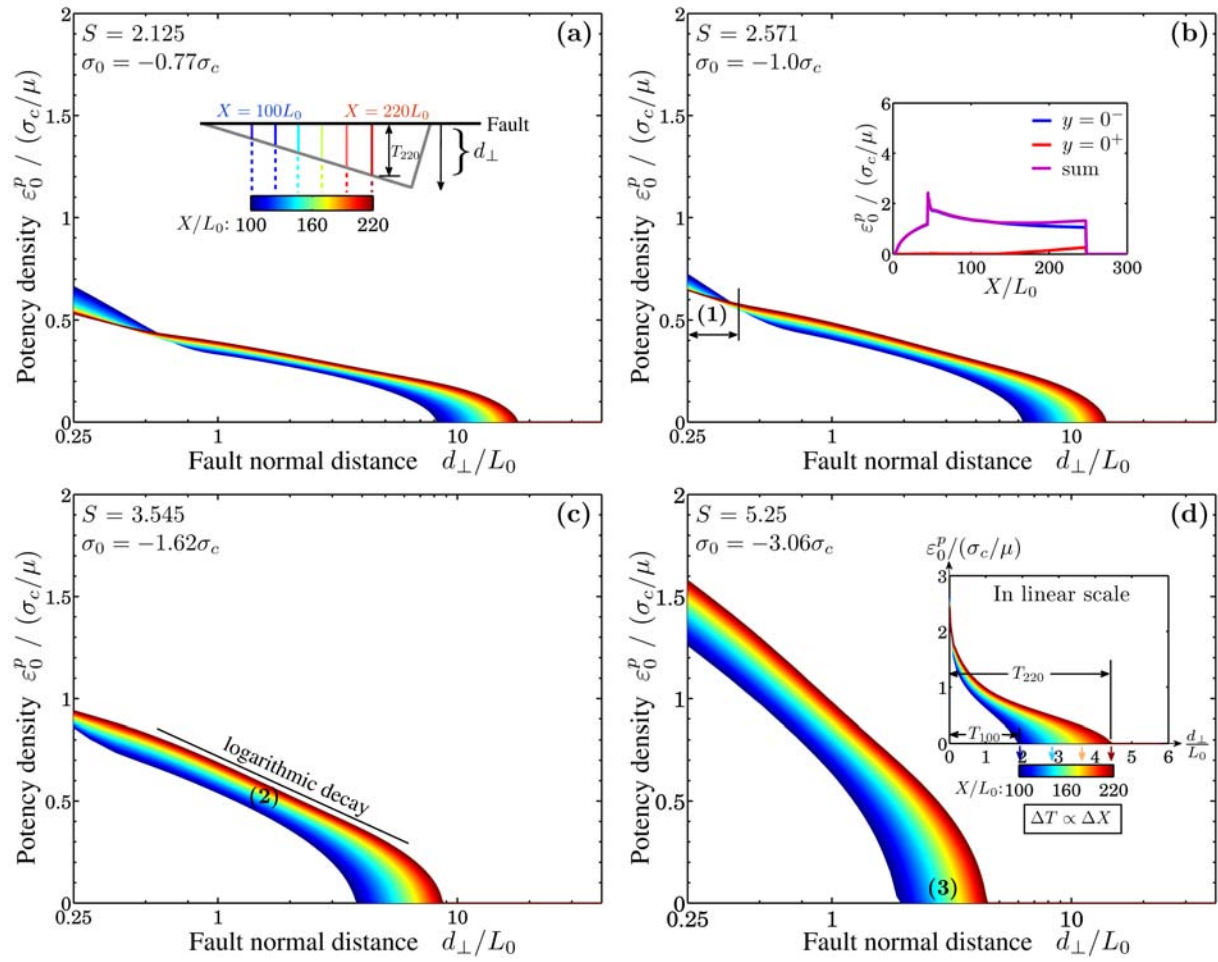


Figure 3

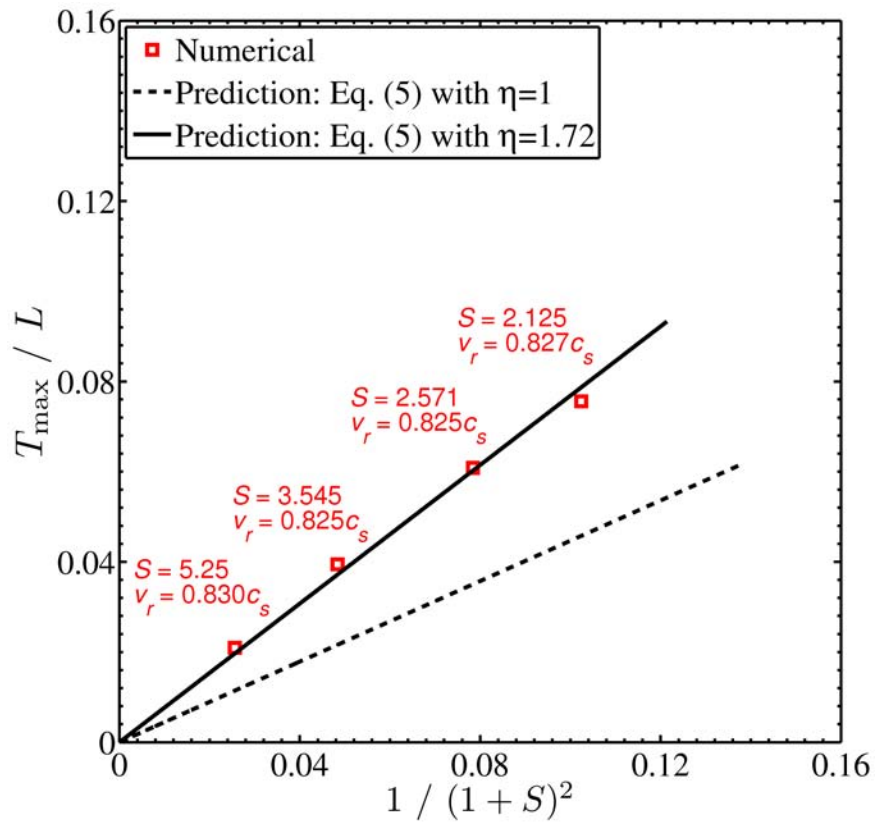


Figure 4

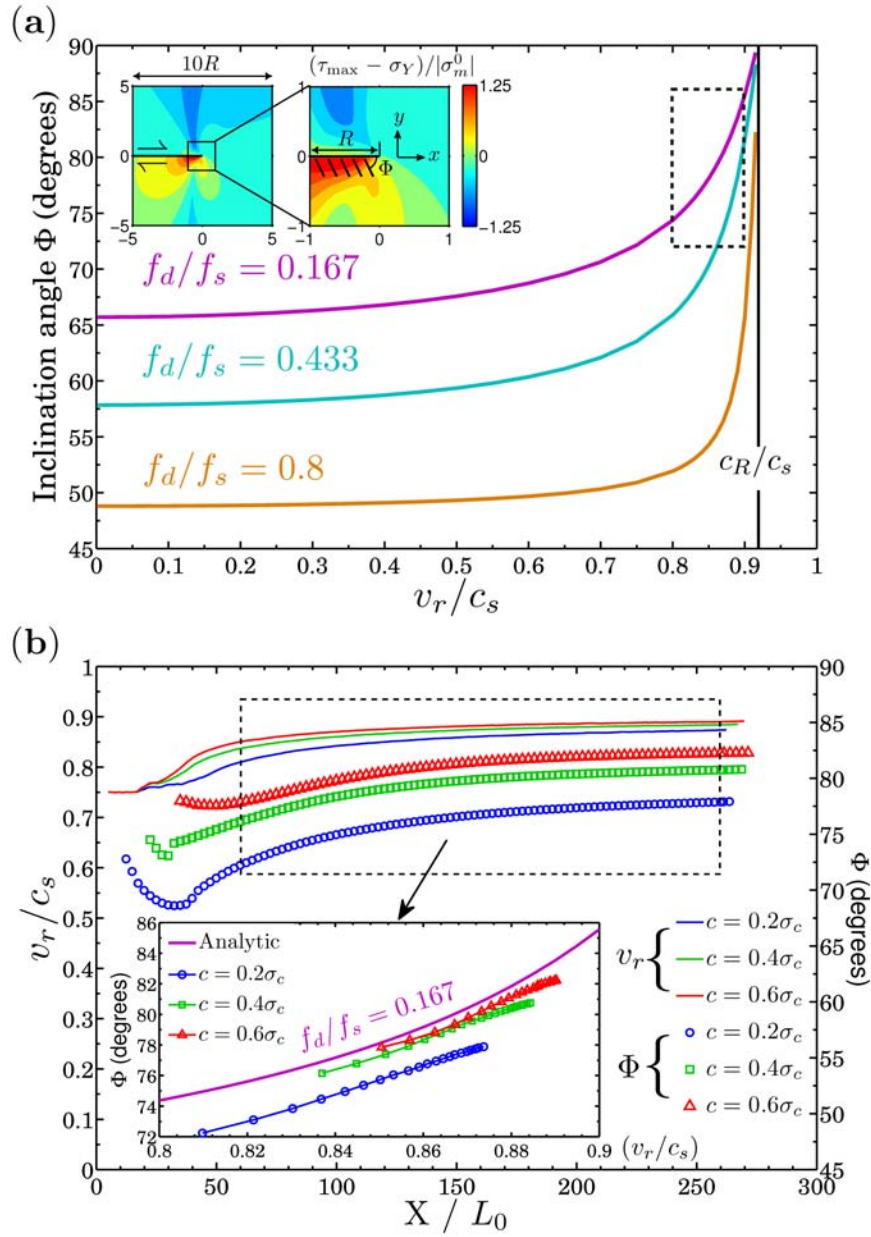


Figure 5

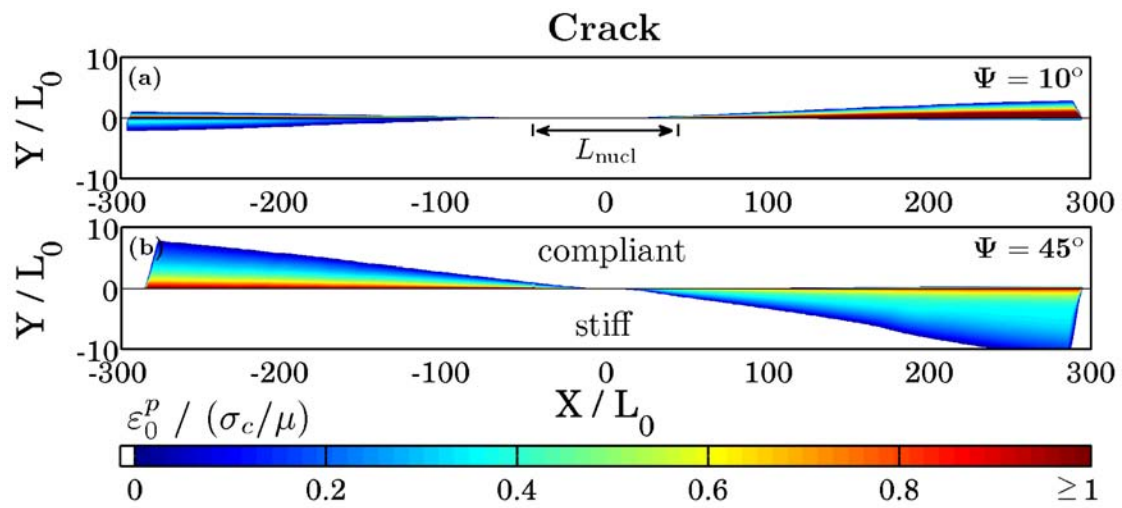


Figure 6

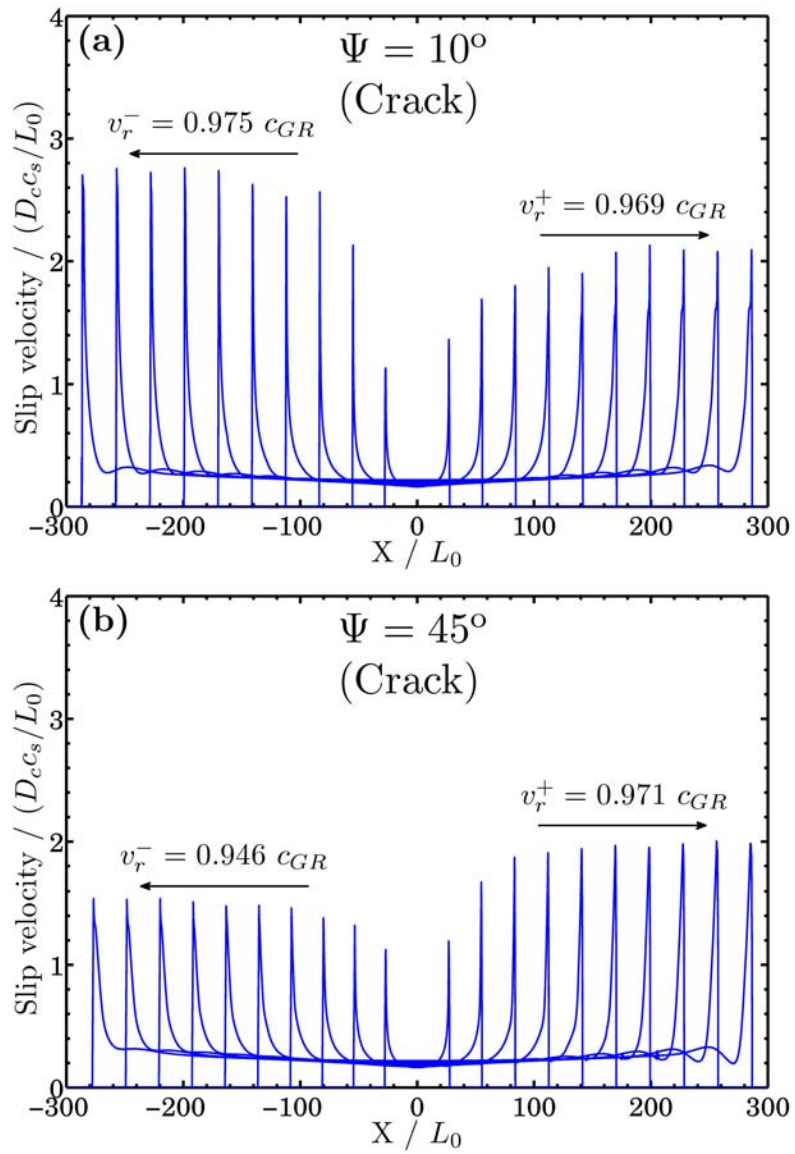


Figure 7

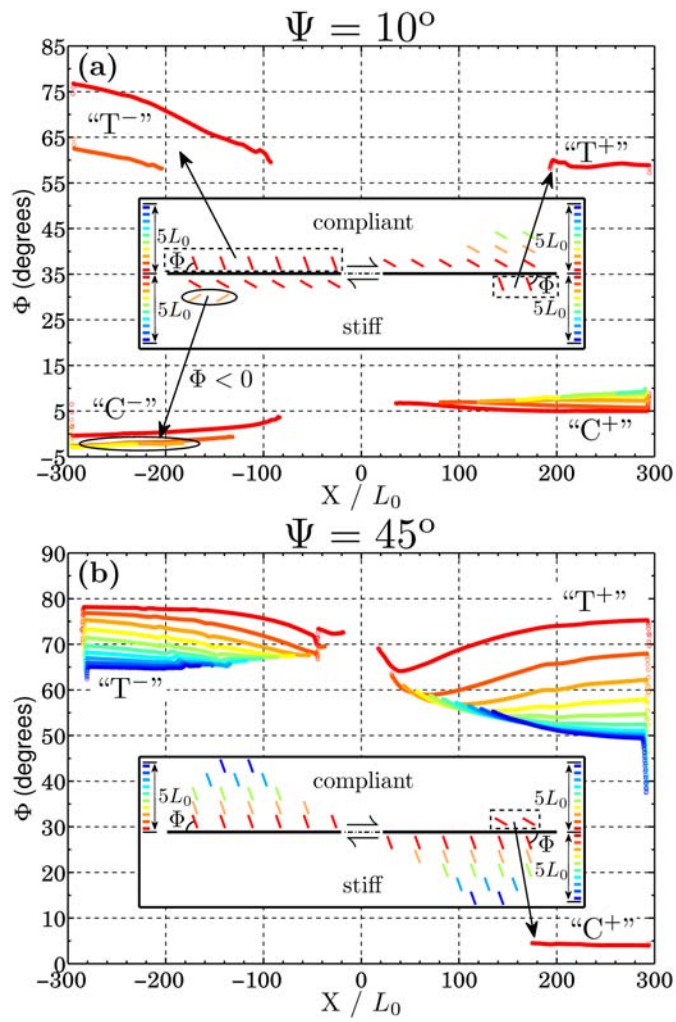


Figure 8

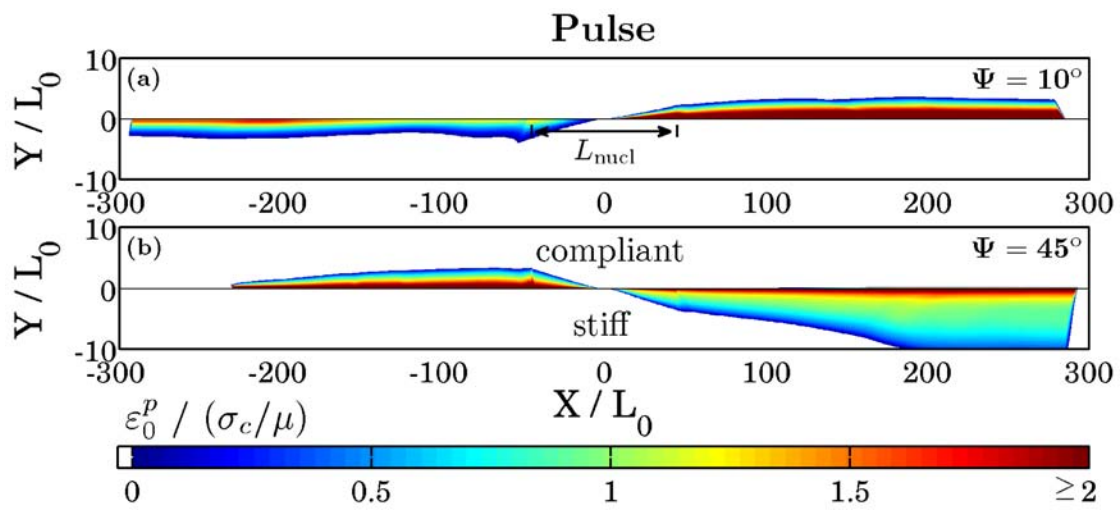


Figure 9

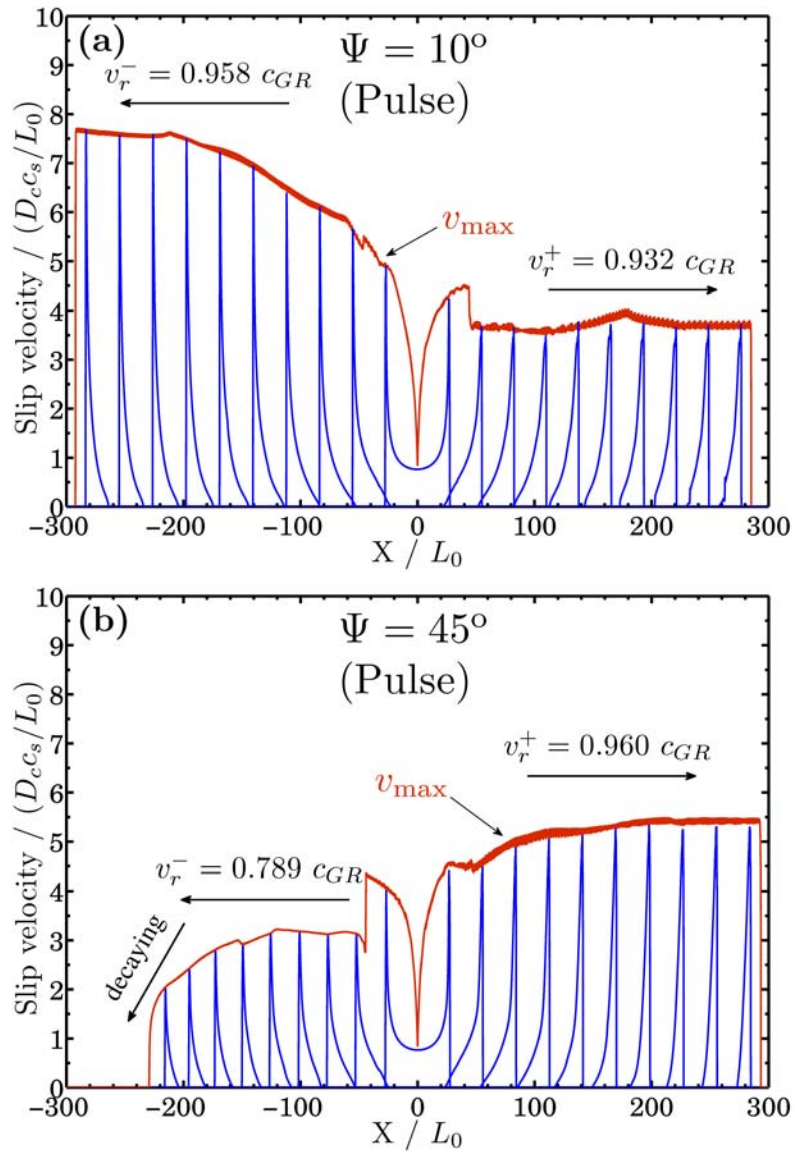


Figure 10

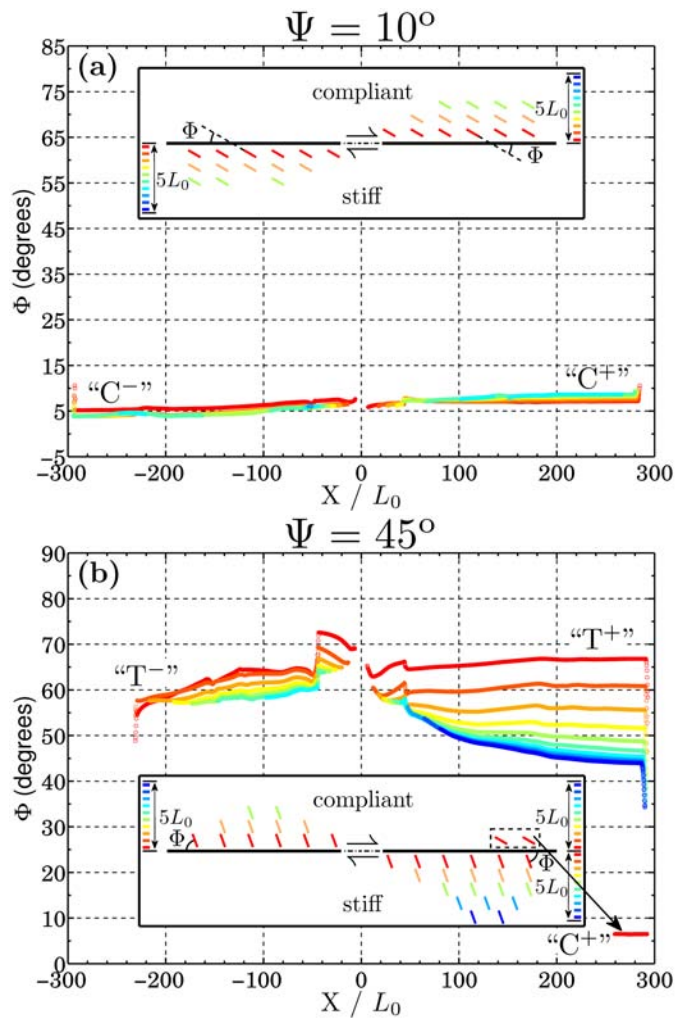


Figure 11

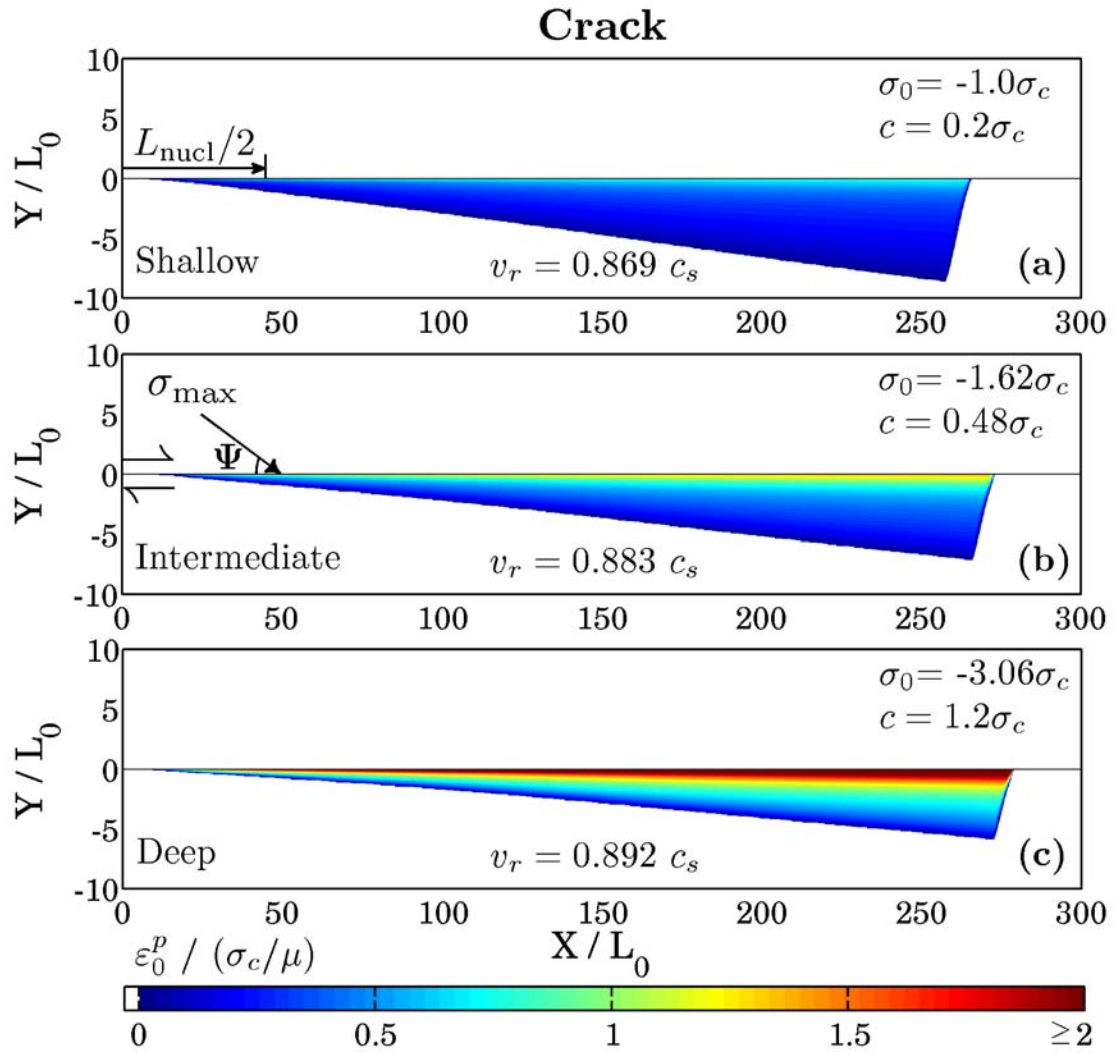


Figure 12

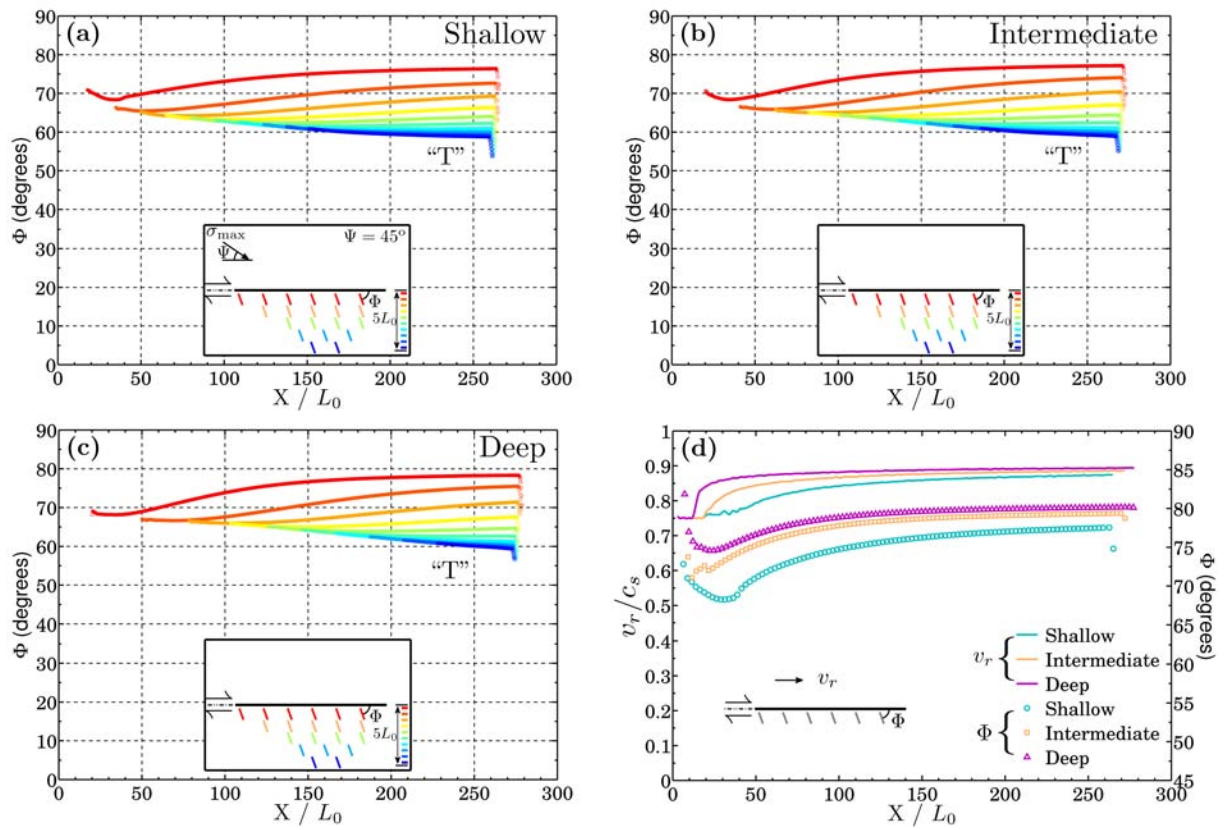


Figure 13

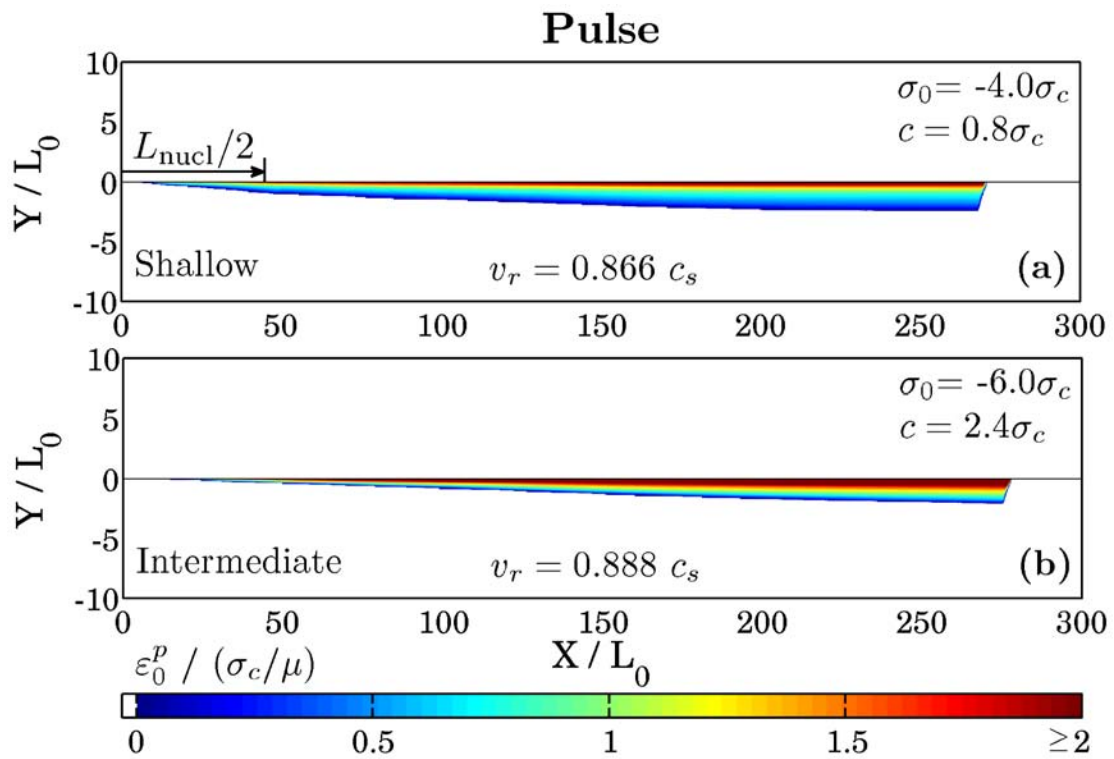


Figure 14

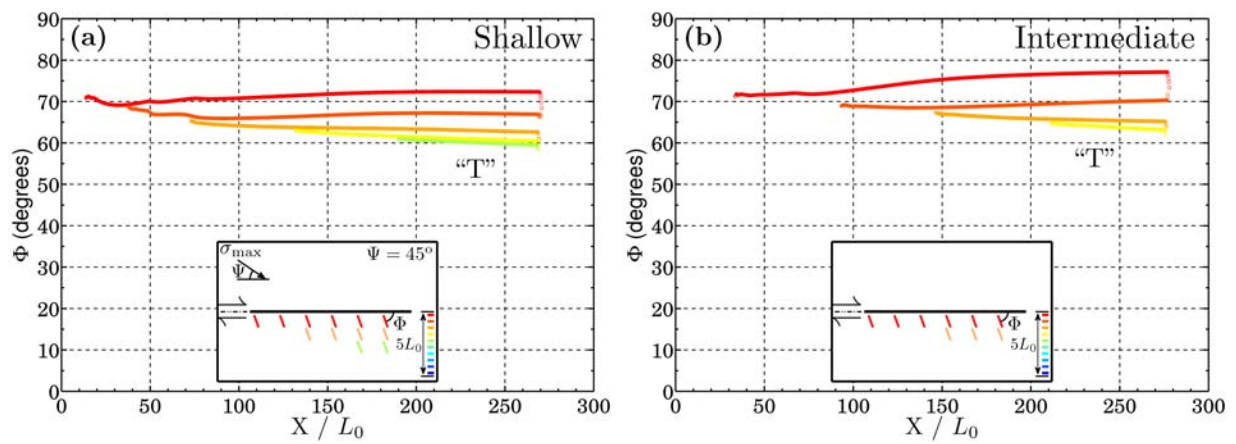


Figure 15

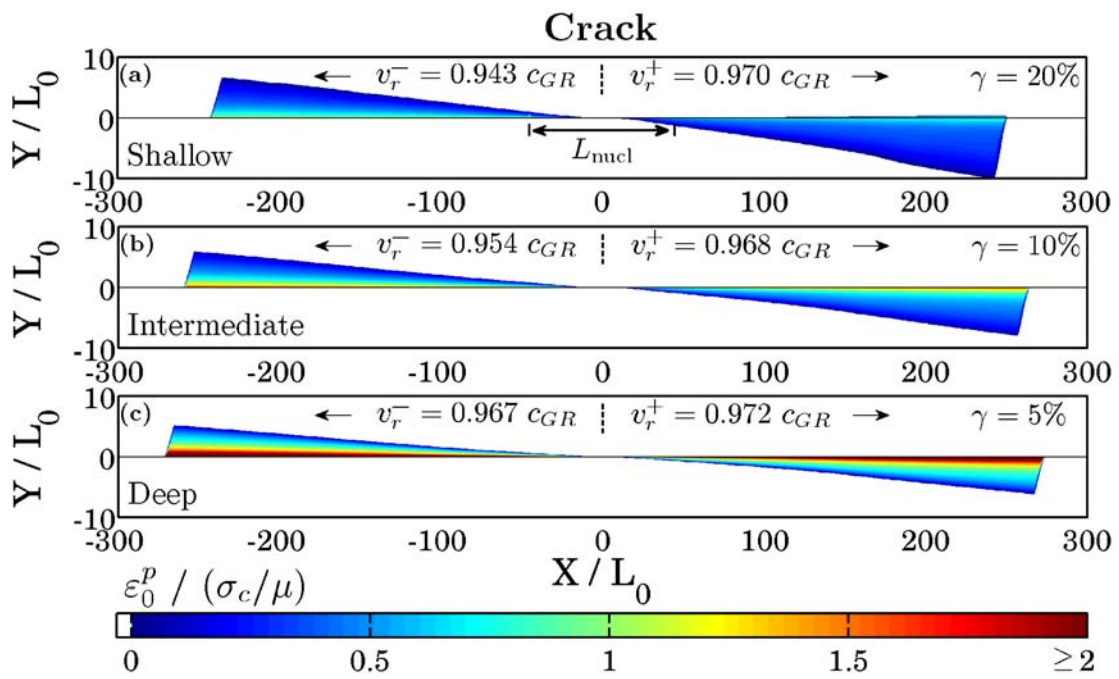


Figure 16

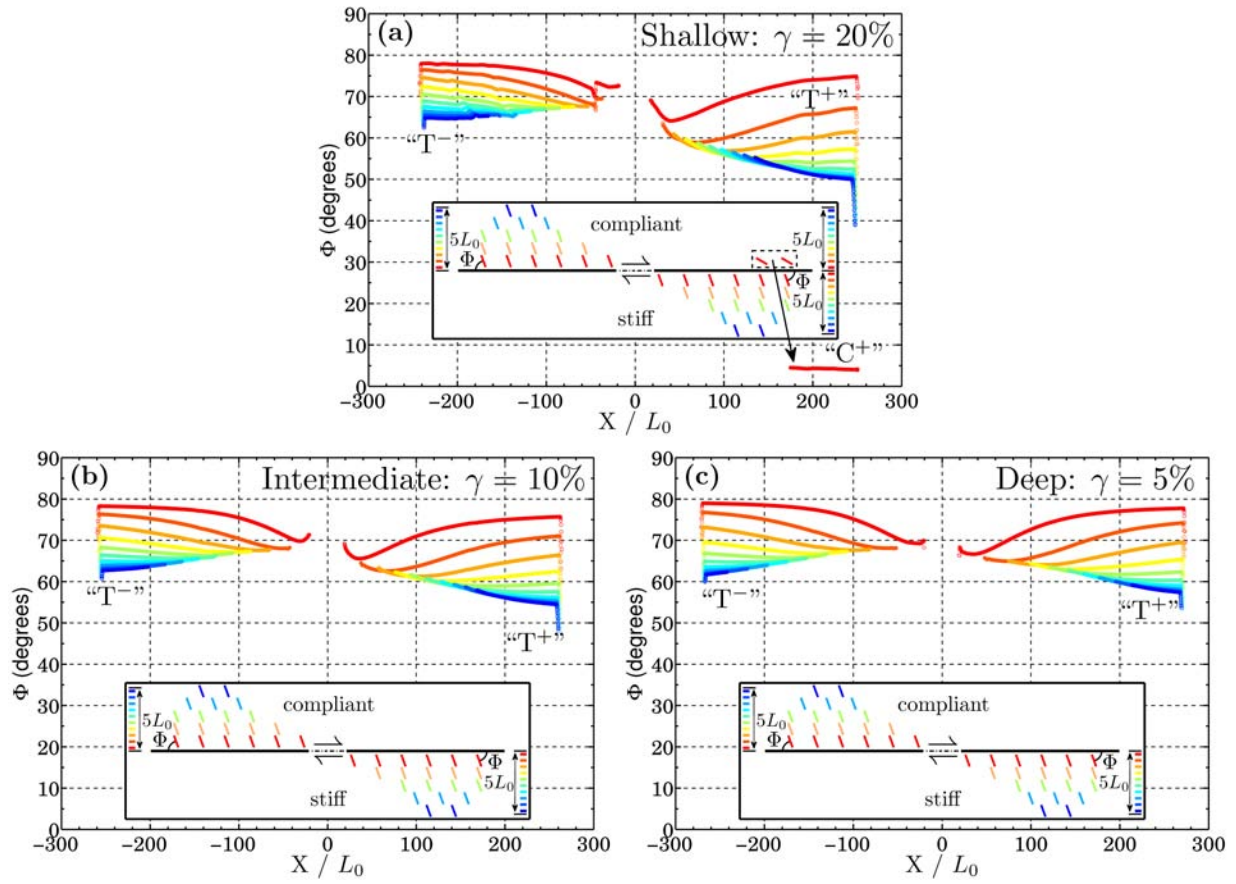


Figure 17

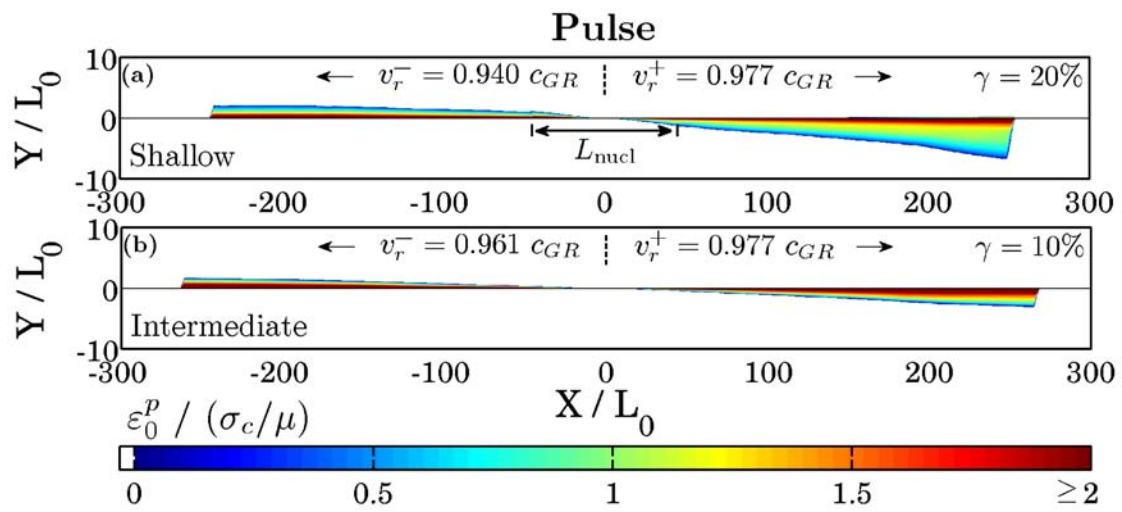


Figure 18

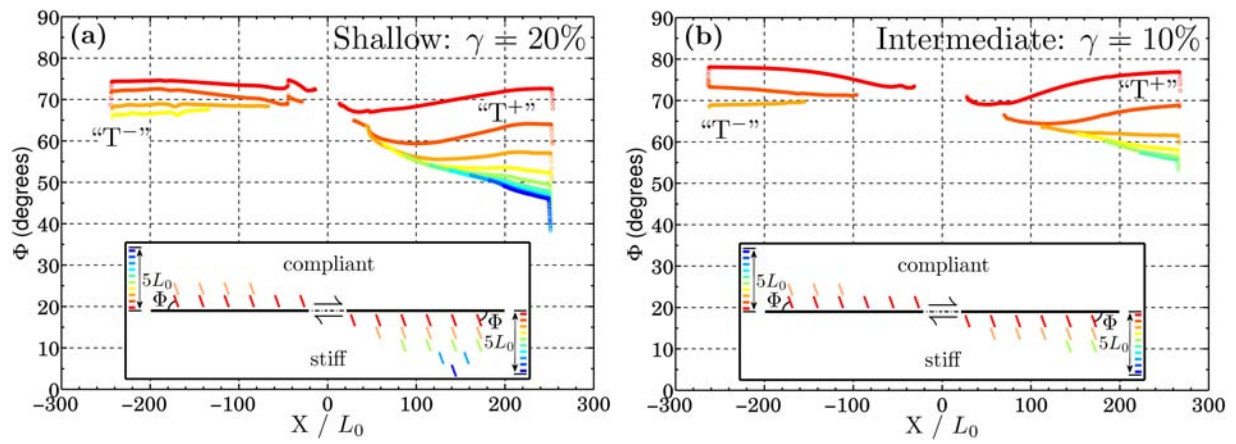


Figure 19